

ABSTRACT

Title: ISOTOPE-ASSISTED METABOLIC FLUX ANALYSIS IN
THE INVESTIGATION OF PROSTATE CANCER

Trevor Graham, Master of Science, 2019

Directed by: Associate Professor Ganesh Sriram
Department of Chemical and Biomolecular Engineering

Understanding cancer metabolism is critical to developing treatment strategies which selectively target malignant cells. Toward this objective, we apply isotope-assisted metabolic flux analysis to the investigation of prostate cancer, which kills over 28,000 men every year in the United States alone.

We performed metabolic flux analysis (MFA) on immortal prostate cancer cell lines to determine the relative activity of metabolic pathways that constitute central carbon metabolism. We identified multiple deviations of the malignant phenotype from that of benign cells. We found that all cell lines exhibited a preference for the pentose phosphate pathway over glycolysis for glucose catabolism, with an average flux partition of $53\% \pm 25\%$ in favor of the pentose phosphate pathway. We also identified a drop in TCA cycle flux from 33.5 ± 10.5 for LNCaP to 19.7 ± 7.8 for CSS90 cells, possibly indicating a preference for glutaminolysis and lipogenesis to fuel rapid proliferation.

ISOTOPE-ASSISTED METABOLIC FLUX ANALYSIS IN THE INVESTIGATION
OF PROSTATE CANCER

By

Trevor Jeremy Graham

Thesis submitted to the Faculty of the Graduate School of the
University of Maryland, College Park in partial fulfillment
of the requirements for the degree of
Master of Science
2019

Advisory Committee:

Associate Professor Ganesh Sriram, Committee Chair

Assistant Professor Amy J. Karlsson

Associate Professor Nam Sun Wang

© Copyright by
Trevor Jeremy Graham
2019

Dedication

To my parents who worked tirelessly to provide the incredible educational opportunities which have been foundational to my personal and professional success.

Acknowledgements

Thank you to Dr. Sriram for introducing me to the field of metabolic engineering; conducting research in this discipline has sparked my interest in the intersection of biology and engineering and driven my professional interests towards biotechnology. Additionally, my colleagues in the metabolic engineering lab have been an invaluable source of information, training and companionship. Dr. Andrew Quinn taught me almost all of the experimental and computational techniques employed in this work. Dr. Navadeep Boruah and Daniel Lugar provided additional insight into computational and analytical techniques.

With respect to this work, I must acknowledge Dr. Navadeep Boruah for the work he contributed in the initial processing of prostate cancer cell line data. None of the cell culture operations would have been possible without the help from our collaborators in Dr. Minhaj Siddiqui's lab at the University of Maryland, Baltimore. De-Xue Fu and Hubert Huang performed cell culture and isotope feeding of prostate cancer cell lines.

Table of Contents

Dedication	ii
Acknowledgements	iii
Abbreviations.....	viii
Chapter 1 : Introduction and Background	1
1.1 Introduction and current detection methods.....	1
1.2 Types of prostate cancer and treatment options.....	2
1.3 Metabolic profile of the prostate.....	4
Chapter 2 : Introduction to Metabolic Engineering Techniques.....	7
2.1 Metabolic engineering theory and background	7
2.2 Computational techniques	18
2.3 Experimental techniques	20
2.4 GC-MS Limitations	22
2.4.1 Conversion of measured compounds to central metabolic precursors	22
2.4.2 Natural abundance correction	23
Chapter 3 : History and Current State of Prostate Cancer Metabolomics Research.....	24
Chapter 4 : Methods, Results and Discussion	34
4.1 Methods	34
4.1.1 Prostate cancer cell line culture and isotope labeling	34
4.1.2 Soluble metabolite extraction	34
4.1.3 Quantification of mass isotopomers by GC-MS	36
4.2 Results and Discussion	37

4.2.1	Prostate cancer cell line data and stationary estimation	37
4.2.2	NMR2Flux+ simulation of central carbon metabolism	43
Chapter 5 : Conclusions and Future Work		54
5.1	Conclusions.....	54
5.2	Future work	55
References		58

List of Tables

Table 2.1 Stoichiometric matrix for the model network.....	12
Table 2.2 Isotopomer balance equations for the network in Figure 2.3.	14

List of Figures

Figure 2.1 Qualitative representation of metabolic and isotopic steady state.	9
Figure 2.2 All possible isotopomers of the amino acid alanine	10
Figure 2.3 Model network containing glycolysis and the pentose phosphate pathway ...	11
Figure 2.4 Predicted Ala[123] and Ala[23] MID for different flux conditions	17
Figure 3.1 General workflow for metabolic phenotype mapping.....	28
Figure 4.1 Enrichment data after 24 hour and 48 hour exposure to ¹³ C medium.	37
Figure 4.2 Comparison of isotopomer abundance data.	38
Figure 4.3 Estimation of stationary enrichment for six metabolite fragments.....	40
Figure 4.4 Parity plot of fitted mass isotopomer abundances vs. measured abundances.	41
Figure 4.5 Box and whisker plot of fitted values for the time constant, τ	42
Figure 4.6 NMR2Flux+ Model 1	43
Figure 4.7 NMR2Flux+ Model 2 and Model 3	44
Figure 4.8 Explanations for NMR2Flux+ input file 2 and input file 4	45
Figure 4.9 Parity plot of simulated mass isotopomer abundances vs. fitted abundances.	47
Figure 4.10 Flux partitioning at central metabolic branch points.....	49
Figure 4.11 Flux solutions for all experimental conditions	51

Abbreviations

3PG, 3-phosphoglycerate

aKG, α -ketoglutarate

ACoA, Acetyl-CoA

ArgSuc, Argininosuccinate

CarbP, Carbamoyl phosphate

Cit, Citrate

Citrul, Citrulline

E4P, Erythrose 4-phosphate

F6P, Fructose 6-phosphate

Fum, Fumarate

G6P, Glucose 6-phosphate

GAP, Glyceraldehyde 3-phosphate

GC-MS, Gas chromatography-mass spectrometry

Gluc, Glucose

Icit, Isocitrate

ILE, Isotope labeling experiment

KEGG, Kyoto Encyclopedia of Genes and Genomes

Mal, Malate

MFA, Metabolic flux analysis

MID, Mass isotopomer distribution

MSTFA, *N*-methyl-*N*-(trimethylsilyl) trifluoroacetamide

MTBSTFA, *N*-methyl-*N*-(*tert*-butyldimethylsilyl) trifluoroacetamide

m/z, mass to charge ratio

NADPH, Nicotinamide adenine dinucleotide phosphate

OAA, Oxaloacetate

P5P Pentose 5-phosphate

PEP, Phosphoenolpyruvate

Pyr, Pyruvate

S7P, Sedoheptulose 7-phosphate

SCoA, Succinyl-coenzyme A

SIM, Selected ion monitoring

SSR, Sum of squared residuals

Succ, Succinate

SVD, Singular value decomposition

TBDMCS, *tert*-butyldimethylchlorosilane

TCA, Tricarboxylic acid

Amino acids are referred to by their standard three letter notation, e.g., alanine (Ala)

The specific carbon atom isotope is denoted [0] for ^{12}C or [1] for ^{13}C . For example, S7P[0011111] indicates the carbon atoms C-1 and C-2 of the seven-carbon (C_7) metabolite sedoheptulose-7-phosphate (S7P) are ^{12}C , while carbon atoms C-3 through C-7 are ^{13}C .

In the context of processing mass spectrometer data for mass fragment identification, bracketed numbers indicate which carbon atoms are contained within a given fragment. e.g. Ala[12] indicates a fragment of alanine containing only the carbon atoms C-1 and C-2. Ala[123] indicates a fragment containing all three carbon atoms of Ala.

Chapter 1 : Introduction and Background

1.1 Introduction and current detection methods

Prostate cancer is one of the most frequently diagnosed malignancies in men around the world. It is consistently one of the most common causes of death in men and a significant financial burden for patients because of diagnostic tests and treatments¹. As of 2012 it is estimated that among all men currently alive, approximately 3% (1 in 33) will die from prostate cancer. This includes over 28,000 deaths in 2012 in the United States alone². Mortality rates have fallen recently due to the development of early screening methods, but there are inherent drawbacks and limitations to the current detection standards.

The most common screening method is a prostate-specific antigen (PSA)-based test, which measures PSA levels in the blood. While PSA screening yields better early detection rates, it also produces false positives and detects malignancies which are indolent². In addition to PSA screening, physicians conduct digital rectal exams which can qualitatively assess prostate normalcy; however, these exams are entirely subjective and somewhat crude. Prostate biopsies are a third option but are invasive, time consuming and costly to the patient; as a result, biopsies are currently not a solution for early detection and are only performed in response to positive results from other screening methods or the emergence of symptoms in the patient³. On top of the aforementioned drawbacks, all early detection methods fail to characterize the specific stage and type of prostate cancer, which limits the prescribing of appropriate treatment methods⁴.

1.2 Types of prostate cancer and treatment options

In almost all cases, tumorigenesis occurs in epithelial cells which comprise the semen-secreting glands inside the prostate. Early stage prostate cancer is localized to small tumors in these glands and becomes more advanced as tumors grow larger. Typical treatment options at this stage include radiotherapy and prostatectomy; however the exact treatment plan is highly dependent on individual circumstances including tumor characteristics and patient life expectancy. In certain patients, active monitoring is sufficient as initially proliferating tumors may remain indolent over the patient's lifetime. Overtreatment and undertreatment are common at this stage because current diagnostic methods are not accurate enough to reliably distinguish indolent from aggressive tumors in all cases⁵.

Advanced prostate cancer is marked by metastasis from the prostate epithelium to secondary sites including lymph nodes and bones. Radiation therapy and surgical methods are ineffective at this stage and hormone therapy remains the only viable option for patients. Prostate cancer proliferation is tied to androgen receptor signaling and thus reducing androgen biosynthesis slows tumor growth⁶. Options for androgen deprivation therapy include surgical castration, downregulation of gonadotropin-releasing hormone and doses of estrogen⁵.

Advanced metastatic prostate cancer can exhibit an altered metabolic phenotype which bypasses the need for androgen receptor signaling and becomes unresponsive to hormone therapy⁷. This "castration-resistant" stage of prostate cancer is difficult to treat and often fatal. Clinical studies have shown limited success with chemotherapy drugs

docetaxel and estramustine, and research is being conducted on a class of immunotherapy drugs including vaccines and monoclonal antibodies⁸.

Current treatment options are largely symptomatic and limited to surgical and extinction procedures for localized tumors and androgen deprivation therapy combined with palliative care for metastasized cases. Easing the burden of prostate cancer will require systemic treatment which stops tumorigenesis but leaves normal prostate cells unaffected. Promising avenues toward the development of such a treatment are fluxomics and metabolomics. Fluxomics requires detailed knowledge of prostate cancer proliferation requirements but can lead to an understanding of the differences between tumor and normal prostate metabolism. Through the same level of metabolic understanding, metabolomics may also identify novel diagnostic markers and help explain the heterogeneity of tumorigenesis observed in patients⁹.

1.3 Metabolic profile of the prostate

It is important to consider the metabolic phenotype of normal prostate cells in order to understand what changes occur in cancerous cells. A main feature of prostate epithelial cells is the accumulation of zinc through upregulation of the zinc transporter ZIP1. High zinc concentrations inhibit m-aconitase, which catalyzes the conversion of citrate to cis-aconitate in the tricarboxylic acid (TCA) cycle. The net effect is low flux through the TCA cycle and an accumulation of citrate, which is secreted by the cells as a component of semen¹⁰. Additionally, zinc inhibits the mitochondrial electron transport chain, which further reduces the energy efficiency of normal prostate epithelial cells. Cancerous mutations must yield significant changes which would allow for the biomass and energy requirements necessary for aggressive proliferation.

Indeed, downregulation of zinc transporter ZIP1 is observed in the early stages of malignant transformation in prostate epithelial cells. This induces a 70-80% reduction in zinc concentration in prostate cancer cells when compared to benign cells¹¹. Lower zinc concentration reverses the inhibition of m-aconitase and marks a shift from a citrate accumulating to citrate oxidizing phenotype. Citrate oxidation through the TCA cycle produces 38 mol ATP/mol glucose consumed, which could fuel the high energy requirements of rapidly proliferating cells. In addition to oxidation, citrate can be shuttled from the mitochondria to the cytosol and cleaved by the enzyme ATP-citrate lyase into oxaloacetate and acetyl-CoA (ACoA). This is the first step in lipogenesis, a process which can fulfill the necessary biomass requirements of proliferating cells. In summary, the shift from benign to malignant phenotype is exemplified by lower intercellular zinc

concentration and an upregulation of the TCA cycle. This shift allows the mutated prostate cells to meet the energy and biomass requirements for cancer to spread.

While key metabolic changes in prostate cancer have been previously identified, it is still unclear what causes the aforementioned shift to a malignant phenotype. One hypothesis links the upregulation of the TCA cycle to increased mutations in mitochondrial DNA (mtDNA)¹². Identifying metabolic differences in benign and cancerous prostate cells may help locate root causes of the malignant shift in prostate cancer cells.

In this work, this problem is studied in a number of novel ways including the application of ¹³C metabolic flux analysis and isotope labeling experiments using human prostate cell lines. First, we introduce core metabolic engineering concepts in **Chapter 2** through fully worked out examples performed on simpler networks. In **Chapter 3**, we review the history of prostate cancer treatment and research, focusing on metabolomics and fluxomics work. We highlight common approaches for studying prostate cancer and how our methods can complement existing research. Next, we introduce our experimental techniques in **Chapter 4. Section 4.1** details all experimental methods, including isotope labeling, metabolite extraction and data processing. In **Section 4.2** We then discuss results from our isotope labeling experiment and nonlinear regression techniques we used to correct for experimental limitations. Fitted data is then used to perform simulations of prostate cancer metabolism to estimate fluxes of central carbon metabolic pathways. We discuss constructing the computational model for simulations and how experimental data limited the scope of the model. Finally, we report flux values and discuss the results, including the insights we gained and areas which can be improved upon in the future.

Chapter 5 summarizes the presented work and we provide guidance for the future direction of this project.

Chapter 2 : Introduction to Metabolic Engineering Techniques

2.1 Metabolic engineering theory and background

A foundational requirement of this work is a rigorous, quantitative definition of the cellular “metabolic phenotype” that can be experimentally probed in a reproducible way. The first step to achieving such a definition is the construction of a metabolic network. Depending on the application, these networks can range in size from a few biochemical reactions to an entire genomic reconstruction. Metabolic networks can be written as a series of balanced chemical reactions which include reactants and products with appropriate stoichiometry, indicating the relative molar quantities of reactant and product which are consumed and produced. Each reaction is assigned a flux value which indicates its activity, or the flow of biological material through it, typically relative to a basis of material which is entering or leaving the metabolic network. By combining stoichiometry and reaction flux values, a series of differential equations can be constructed which collectively represent any given metabolic network. For any metabolite M , the differential equation describing the time evolution of its concentration is written as:

$$\frac{dM_i}{dt} = \sum_j S_{ij} v_j \quad (1)$$

where v_j is the flux of reaction j , S_{ij} is the stoichiometric coefficient and $\frac{dM_i}{dt}$ is the change in concentration of metabolite M with respect to time.

More complex genome scale networks are curated by synthesizing available metabolic and genomic information from a particular organism using databases such as Metacyc¹³ and KEGG¹⁴. The experimental and computational processes carried out on

these constructed metabolic networks have the end goal of quantifying the flux values for each reaction and are encompassed in an approach called metabolic flux analysis (MFA).

A common experimental methodology for MFA involves the use of isotopically “labeled” carbon atoms (i.e. ^{13}C), which can be distinguished from naturally abundant ^{12}C and tracked as they move through metabolism. Introducing and measuring the presence of these isotopes is encompassed in an isotope labelling experiment (ILE). ILEs are conducted by feeding a grown population of cells an isotopically labeled carbon source. As the cell population grows, it produces metabolites which contribute to a metabolite pool which becomes more saturated with ^{13}C atoms over time. There are two important dynamics to consider with respect to the metabolite pool: how the pool size changes and how the labeling of the pool changes. These dynamics are illustrated in **Figure 2.1** using a simple linear reaction network of compounds containing three carbon atoms. A changing pool size of metabolic intermediates indicates the cell population is not operating under a single metabolic phenotype (metabolic steady state). Changing labeling patterns of specific metabolites in the pool indicates that the population is not at isotopic steady state. It is critical to account for both metabolic and isotopic steady states when performing MFA; the effect of these conditions on the mathematical complexity of network modeling is discussed below within the larger example network (**Figure 2.3**).

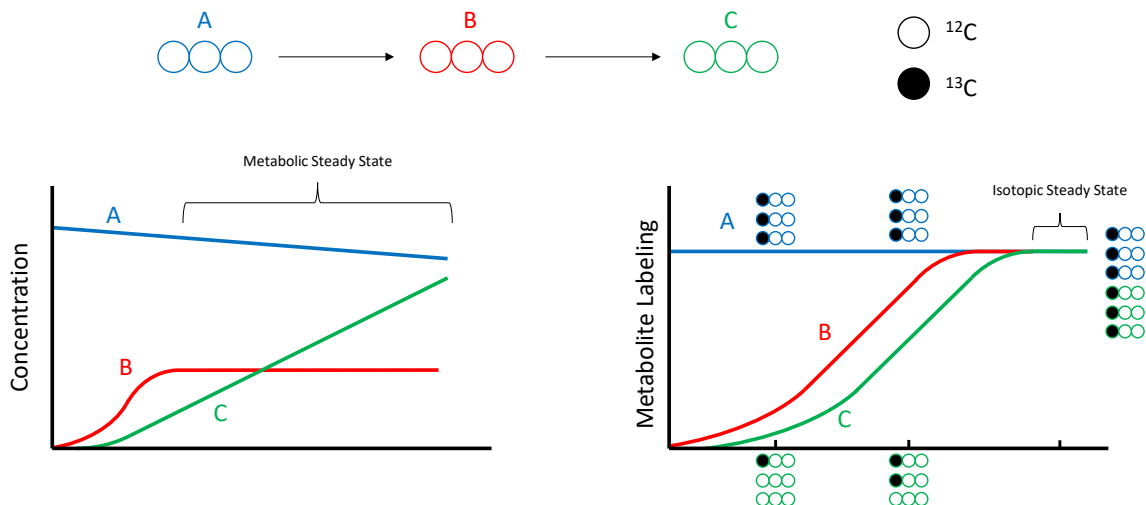


Figure 2.1 Qualitative representation of metabolic and isotopic steady state. Approximate changes in the size of the metabolite pools (left) and labeling of the metabolite pools (right) for a linear reaction network which initially only contains metabolite A. Metabolic steady state is achieved when the change in concentration with respect to time is 0 for intermediate metabolites and isotopic steady state is achieved when the labeling of each metabolite is constant.

In order to quantify metabolite labeling information and apply that information to the previously described quantitative definition of a metabolic network, it is necessary to introduce the concept of isotopomers. Isotopomers are isotopic isomers, or variants of a single metabolite that contain a unique pattern of isotopically labeled atoms. For any given metabolite there are 2^n possible isotopomers, where n is the number of atoms which may become isotopically labeled. While many different elements may be used in ILEs (nitrogen, oxygen, etc.) the remainder of this work will focus solely on carbon labeling. Any metabolite with 3 carbon atoms has $2^3 = 8$ possible isotopomers, as seen in **Figure 2.2** which depicts all isotopomers of the amino acid alanine.

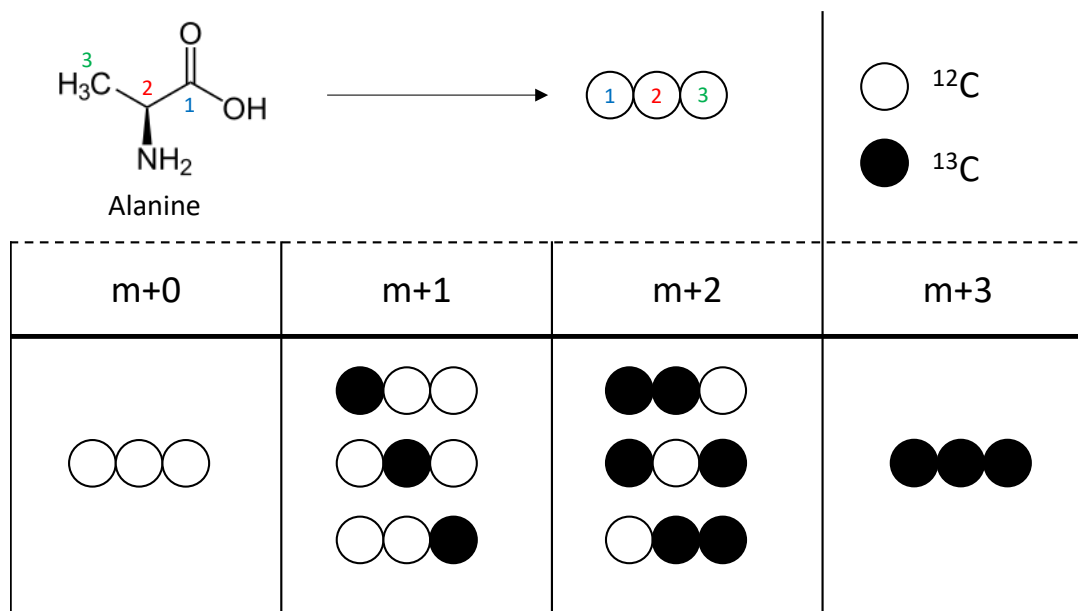


Figure 2.2 All possible isotopomers of the amino acid alanine. Each isotopomer is categorized by the number of ^{13}C atoms it contains, or the number of additional atomic mass units it possesses. For example, there are three isotopomers with one ^{13}C atom and thus are categorized as m+1, or “mass plus one”.

By taking into account all of the possible isotopomers that are formed in a metabolic network, a series of isotopomer balances can be constructed which facilitate the transfer of information from ILEs to constructed metabolic models.

The primary output of any ILE is the labeling information and experiment design must be carried out such that the appropriate amount of labeling information is obtained. Parameters of experiment design for ILEs include the type of substrate being fed, the specific labeling of the substrate, the number of measurements and the temporal spacing of each measurement. It will be useful to consider a simplified example in order to understand how labeling information is obtained, applied and how it can be affected by changing experimental parameters.

Here, we examine two different pathways that metabolize glucose: glycolysis and the pentose phosphate pathway. These pathways diverge at the metabolite glucose-6-phosphate (G6P) and the relative flux of G6P through each pathway gives information about the overall metabolic phenotype of cellular glucose catabolism. All reactions in this model (**Figure 2.3**) are considered irreversible and the natural abundance of ^{13}C is considered negligible.

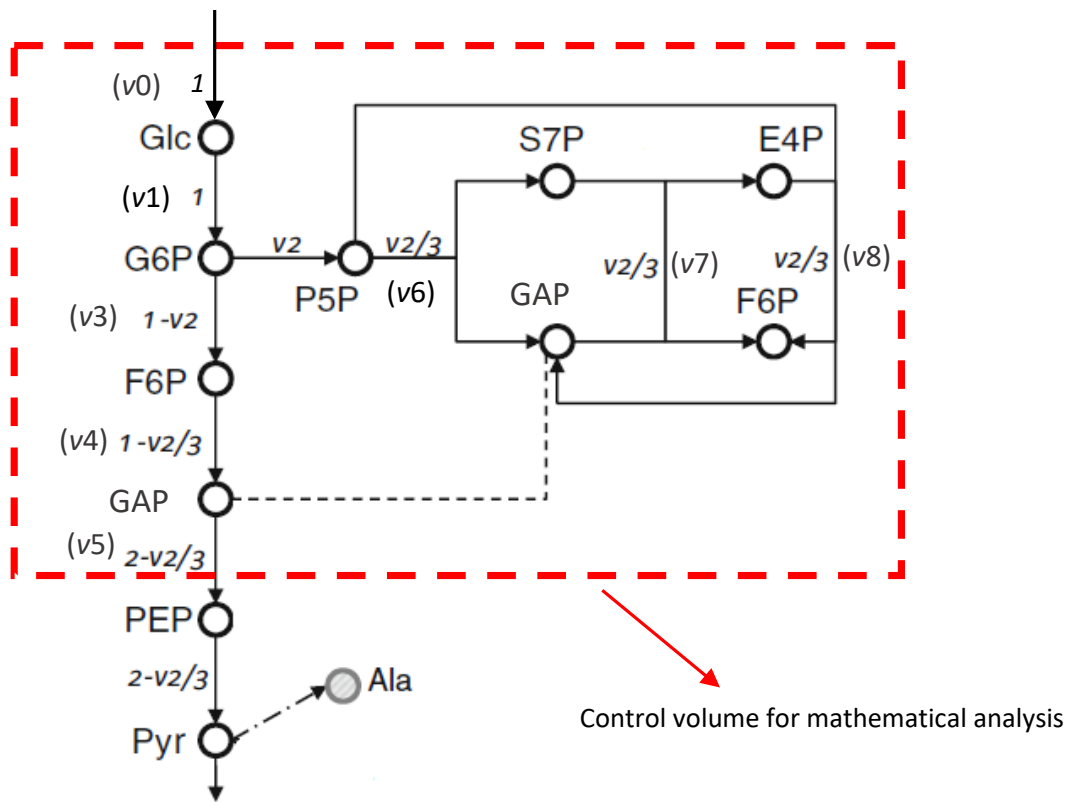


Figure 2.3 Model network containing glycolysis and the pentose phosphate pathway. Each reaction is assigned a unique number and a flux value in terms of the independent fluxes " v_2 " and " v_0 ". The red box outlines the control volume where the mass balance and degree of freedom calculations are contained. All outside fluxes are dependent on results inside the control volume and do not need to be solved. Figure adapted with permission from Zheng and Sriram.¹⁵

The network in **Figure 2.3** can be written as a stoichiometric matrix S , where the columns represent reactions and the rows represent the stoichiometry of the metabolites involved in each reaction. The stoichiometric matrix for this network is shown in **Table 2.1**.

Table 2.1 Stoichiometric matrix for the model network. Reaction stoichiometry is taken from gene annotation data.

	v0	v1	v2	v3	v4	v5	v6	v7	v8
Gluc	1	-1	0	0	0	0	0	0	0
G6P	0	1	-1	-1	0	0	0	0	0
F6P	0	0	0	1	-1	0	0	1	-1
P5P	0	0	1	0	0	0	-2	0	1
S7P	0	0	0	0	0	0	1	-1	0
E4P	0	0	0	0	0	0	0	1	-1
GAP	0	0	0	0	2	-1	1	-1	1

Multiplying this matrix with a flux vector v yields the governing mass balance matrix equation for a given metabolic network,

$$S_{ij} v_j = \frac{dC_i}{dt} \quad (2)$$

Equation 2 is simply a collection of each metabolite's mass balance (Equation 1). If a cell population is at metabolic steady state, the metabolite concentration is constant and the differential equations collected in Equation 2 are reduced to algebraic equations of the form:

$$S_{ij} v_j = 0 \quad (3)$$

The mass balances and stoichiometric matrix for a given network indicate the flux dependence between biochemical reactions and can help identify independent and dependent fluxes, which are related by a degree of freedom (DOF) calculation as follows:

$$\begin{aligned} \text{DOF} &= \text{Total number of fluxes} \\ &\quad - \text{Number of intracellular metabolites} \\ &\quad - \text{Number of extracellular fluxes} \end{aligned} \quad (4)$$

This DOF calculation holds for linearly independent metabolite balances only. Note that in **Figure 2.3**, phosphoenolpyruvate (PEP) and pyruvate (Pyr) were excluded from the mathematical formulation of the network. Because of the way fluxes are designated, PEP and Pyr metabolite balances are linearly dependent on the glyceraldehyde 3-phosphate (GAP) metabolite balance and thus should not be included in DOF calculations. To verify independence of metabolite balances, we compare the rank of the stoichiometric matrix with the number of rows. If the rank is less than the number of rows, there are dependent balances which should be removed. For the network in Table 1, which has 9 fluxes and 7 metabolites, the DOF is 2. The DOF equals the number of independent fluxes; these can be used as variables to express the remaining dependent fluxes. A typical choice is to set an incoming flux as a basis for the rest of the network; in this model glucose uptake (v_0) is normalized to 1. The second chosen free flux is v_2 , the entrance of G6P into the pentose phosphate pathway. Algebraic manipulation of the metabolite balances in **Table 2.1** transforms all flux variables into functions of the incoming glucose flux and v_2 (see **Figure 2.3**). However, the flux v_2 remains undetermined. To determine it and thus, to determine the remaining fluxes in the network,

isotopomer balances must be formulated by following the flow of labels through the system.

Each metabolite in a given network can be written as a set of isotopomers, which may be formed given the specific labeling of the fed substrate. In this example, glucose is the substrate and will be fed in a mixture that is both unlabeled and uniformly labeled with ^{13}C at all 6 carbon atoms. One experimental choice to consider is the ratio of unlabeled to labeled glucose fed. The mixture composition will affect the labeling patterns extracted from an ILE. Isotopomer balances are written on isotopomers in a similar fashion to metabolite balances, but with terms that represent isotopomer abundance. The isotopomer balance at metabolic steady state is

$$\sum S v A = 0 \quad (5)$$

where A is the isotopomer abundance vector. For any given metabolite, the sum of its isotopomer abundances is 1. It is critical that the cell population is under isotopic steady state (**Figure 2.1**), otherwise A will be dependent on time and flux calculation becomes much more difficult. A complete list of isotopomers and respective balances for the network in **Figure 2.3** is available in **Table 2.2**.

Table 2.2 Isotopomer balance equations for the network in Figure 2.3. For a given set of independent variables, simultaneous evaluation of these balances gives the set of all corresponding flux solutions and isotopomer abundances for the network.

Isotopomer	Production	Consumption
G6P ₀₀₀₀₀₀		$p = \text{G6P}_{000000}$
G6P ₁₁₁₁₁₁		$(1-p) = \text{G6P}_{111111}$
P5P ₀₀₀₀₀	$v_2[\text{G6P}_{000000}]$	$= v_2[\text{P5P}_{00000}]$
P5P ₁₁₁₁₁	$v_2[\text{G6P}_{11111}]$	$= v_2[\text{P5P}_{11111}]$
S7P ₀₀₀₀₀₀₀	$v_6[\text{P5P}_{00000}][\text{P5P}_{00000}]$	$= v_6[\text{S7P}_{0000000}]$
S7P ₁₁₁₁₁₁₁	$v_6[\text{P5P}_{11111}][\text{P5P}_{11111}]$	$= v_6[\text{S7P}_{1111111}]$
S7P ₀₀₁₁₁₁₁	$v_6[\text{P5P}_{00000}][\text{P5P}_{11111}]$	$= v_6[\text{S7P}_{0011111}]$

S7P ₁₁₀₀₀₀₀	$v6[P5P_{11111}][P5P_{00000}] = v6[S7P_{1100000}]$
E4P ₀₀₀₀	$v7((GAP_{000})([S7P_{0000000}] + [S7P_{1100000}] + [GAP_{111})([S7P_{0000000}] + [S7P_{1100000}] + [GAP_{011})([S7P_{0000000}] + [S7P_{1100000}] + [GAP_{100})([S7P_{0000000}] + [S7P_{1100000}] + [GAP_{001})([S7P_{0000000}] + [S7P_{1100000}] + [GAP_{110})([S7P_{0000000}] + [S7P_{1100000}])))) = v7[E4P_{0000}]$
E4P ₁₁₁₁	$v7((GAP_{000})([S7P_{1111111}] + [S7P_{0011111}] + [GAP_{111})([S7P_{1111111}] + [S7P_{0011111}] + [GAP_{011})([S7P_{1111111}] + [S7P_{0011111}] + [GAP_{100})([S7P_{1111111}] + [S7P_{0011111}] + [GAP_{001})([S7P_{1111111}] + [S7P_{0011111}] + [GAP_{110})([S7P_{1111111}] + [S7P_{0011111}])))) = v7[E4P_{1111}]$
F6P ₀₀₀₀₀₀	$v3[G6P_{000000}] + v7([GAP_{000}][S7P_{0000000}] + v8([E4P_{0000}][P5P_{00000}]) = v4[F6P_{000000}]$
F6P ₁₁₁₁₁₁	$v3[G6P_{111111}] + v7([GAP_{111}][S7P_{1111111}] + v8([E4P_{1111}][P5P_{11111}]) = v4[F6P_{111111}]$
F6P ₁₁₁₀₀₀	$v7[GAP_{000}][S7P_{1111111}] = v4[F6P_{111000}]$
F6P ₀₀₀₁₁₁	$v7[GAP_{111}][S7P_{0000000}] = v4[F6P_{000111}]$
F6P ₁₁₀₀₀₀	$v7[GAP_{000}][S7P_{1100000}] = v4[F6P_{110000}]$
F6P ₁₁₀₁₁₁	$v7[GAP_{111}][S7P_{1100000}] = v4[F6P_{110111}]$
F6P ₀₀₁₀₀₀	$v7[GAP_{000}][S7P_{0011111}] = v4[F6P_{001000}]$
F6P ₀₀₁₁₁₁	$v7[GAP_{111}][S7P_{0011111}] = v4[F6P_{001111}]$
F6P ₀₀₀₀₁₁	$v7[GAP_{011}][S7P_{0000000}] = v4[F6P_{000011}]$
F6P ₁₁₁₀₁₁	$v7[GAP_{011}][S7P_{1111111}] = v4[F6P_{111011}]$
F6P ₁₁₀₀₁₁	$v7[GAP_{011}][S7P_{1100000}] = v4[F6P_{110011}]$
F6P ₀₀₁₀₁₁	$v7[GAP_{011}][S7P_{0011111}] = v4[F6P_{001011}]$
F6P ₀₀₀₁₀₀	$v7[GAP_{100}][S7P_{0000000}] = v4[F6P_{000100}]$
F6P ₁₁₁₁₀₀	$v7[GAP_{100}][S7P_{1111111}] = v4[F6P_{111100}]$
F6P ₁₁₀₁₀₀	$v7[GAP_{100}][S7P_{1100000}] = v4[F6P_{110100}]$
F6P ₀₀₁₁₀₀	$v7[GAP_{100}][S7P_{0011111}] = v4[F6P_{001100}]$
F6P ₀₀₀₀₀₁	$v7[GAP_{001}][S7P_{0000000}] + v8[E4P_{1111}][P5P_{00000}] = v4[F6P_{000001}]$
F6P ₁₁₁₀₀₁	$v7[GAP_{001}][S7P_{1111111}] = v4[F6P_{111001}]$
F6P ₁₁₀₀₀₁	$v7[GAP_{001}][S7P_{1100000}] = v4[F6P_{110001}]$
F6P ₀₀₁₀₀₁	$v7[GAP_{001}][S7P_{0011111}] = v4[F6P_{001001}]$
F6P ₀₀₀₁₁₀	$v7[GAP_{110}][S7P_{0000000}] = v4[F6P_{000110}]$
F6P ₁₁₁₁₁₀	$v7[GAP_{110}][S7P_{1111111}] + v8[E4P_{0000}][P5P_{11111}] = v4[F6P_{111110}]$
F6P ₁₁₀₁₁₀	$v7[GAP_{110}][S7P_{1100000}] = v4[F6P_{110110}]$
F6P ₀₀₁₁₁₀	$v7[GAP_{110}][S7P_{0011111}] = v4[F6P_{001110}]$
GAP ₀₀₀	$v4(2[F6P_{000000}] + [F6P_{111000}] + [F6P_{110000}] + [F6P_{001000}] + [F6P_{000011}] + [F6P_{000100}] + [F6P_{000001}] + [F6P_{000110}] + v8[E4P_{0000}] + v6([P5P_{00000}]^2 + [P5P_{00000}][P5P_{11111}])) = v5[GAP_{000}]$
GAP ₁₁₁	$v4(2[F6P_{111111}] + [F6P_{111000}] + [F6P_{110111}] + [F6P_{001111}] + [F6P_{111011}] + [F6P_{111100}] + [F6P_{111001}] + [F6P_{111110}] + v8[E4P_{1111}] + v6([P5P_{11111}]^2 + [P5P_{00000}][P5P_{11111}])) = v5[GAP_{111}]$
GAP ₀₁₁	$v4([F6P_{110000}] + [F6P_{110111}] + [F6P_{000011}] + [F6P_{111011}] + 2[F6P_{110011}] + [F6P_{001011}] + [F6P_{110100}] + [F6P_{110001}] + [F6P_{110110}]) = v5[GAP_{011}]$
GAP ₁₀₀	$v4([F6P_{001000}] + [F6P_{001111}] + [F6P_{001011}] + [F6P_{000100}] + [F6P_{111100}] + [F6P_{110100}] + 2[F6P_{001100}] + [F6P_{001001}] + [F6P_{001110}]) = v5[GAP_{100}]$
GAP ₀₀₁	$v4([F6P_{000001}] + [F6P_{111001}] + [F6P_{110001}] + [F6P_{001001}]) = v5[GAP_{001}]$
GAP ₁₁₀	$v4([F6P_{000110}] + [F6P_{111110}] + [F6P_{110110}] + [F6P_{001110}]) = v5[GAP_{110}]$

Isotopomer formation is often dependent on the abundance of more than one precursor isotopomer which creates nonlinearity in the system of isotopomer balances. For example, the formation of $S7P0011111$ through reaction $v6$ is dependent on both $P5P00000$ and $P5P11111$, leading to the following nonlinear isotopomer balance:

$$v6 * [P5P00000][P5P11111] - v7 * [S7P0011111] = 0 \quad (6)$$

The simplest way to transform these nonlinear balances is the substitution of isotopomer abundances which can be pre-solved using other balances in the network. The balances for $P5P00000$ and $P5P11111$ are written as:

$$v2 * [G6P000000] - v2 * [P5P00000] = v2 * p - v2 * [P5P00000] = 0 \quad (7)$$

$$v2 * [G6P111111] - v2 * [P5P11111] = v2 * (1 - p) - v2 * [P5P11111] = 0 \quad (8)$$

where p is an design parameter representing the fraction of U-¹²C glucose fed to the system. Simple rearrangement allows for the explicit solution of both isotopomer abundances, which can be substituted back into equation 6

$$v6 * p * (1 - p) - v7 * [S7P0011111] = 0 \quad (9)$$

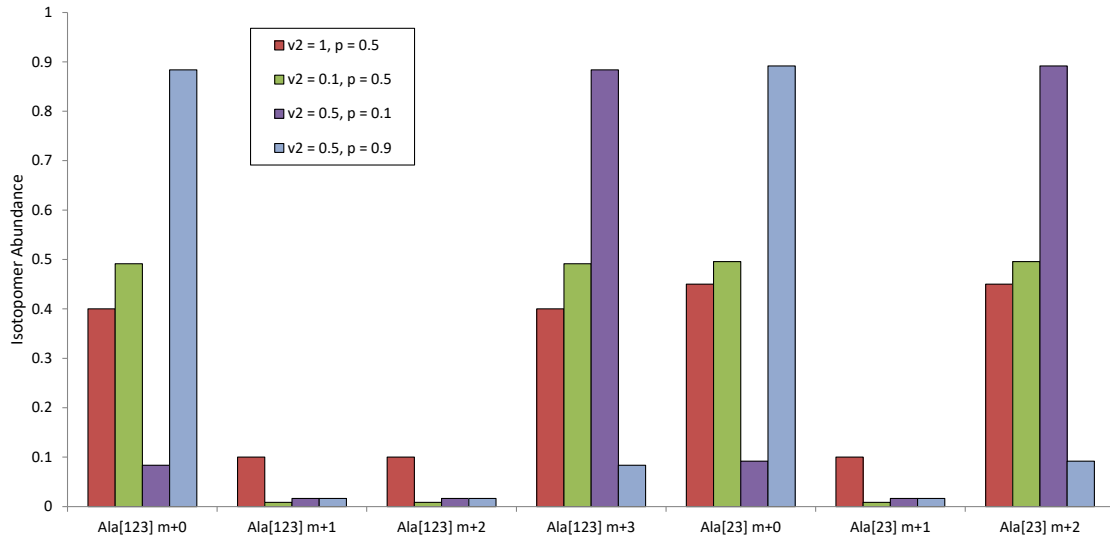


Figure 2.4 Predicted Ala[123] and Ala[23] MID for different flux conditions. “v2” is the fraction of carbon flowing through the pentose phosphate pathway; “p” is the fraction of unlabeled ^{12}C glucose fed. Ala MID are directly predicted from GAP MID obtained via solving mass balances.

This simple solution methodology may become impossible when multiple nonlinear balances are dependent on one another. If the formation of P5P was dependent on multiple precursor metabolites, substitutions would lead to a different set of nonlinear balances. Strategies for handling and linearizing such interdependent networks are discussed in **Section 2.2**. Simultaneous evaluation of all linearized balance equations gives the abundance of each isotopomer for a given ratio of $\text{U-}^{13}\text{C}/\text{U-}^{12}\text{C}$ glucose fed. Summation of the appropriate GAP isotopomers gives a prediction for the MID of alanine which would reflect the metabolic phenotype of the network. **Figure 2.4** shows how the predicted MID of alanine changes depending on the experimental conditions and flux mode of the network.

2.2 Computational techniques

Explicit solutions to isotopomer abundances are not always easily obtainable; most networks usually require the application of a rigorous technique to linearize isotopomer balances. Isotopomers can be transformed into cumomers¹⁶, bondomers¹⁷ (when a sole carbon source is used in U-¹³C and naturally abundant forms) and elementary metabolite units¹⁸, all of which allow for the expression of networks in terms of a cascade of linear equations. Cumomer balancing is the basis for flux analysis in the flux evaluation computer program developed by Dr. Sriram, NMR2Flux+¹⁹. The program follows the general approach outlined above; first all dependent flux values are computed based on the stoichiometric network and independent flux values inputted by the user. Cumomer balances are then computed, solved and transformed into isotopomer abundances. These abundances are compared to measured abundances by computing the global sum of square residuals (SSR). A simulated annealing optimization algorithm is employed to minimize the SSR by varying the independent fluxes. This method uses reaches a global minimum SSR by utilizing a temperature-dependent random walk until a designated stop point is reached²⁰.

Once a set of fluxes is found that optimally accounts for the experimental labeling measurements, bootstrap simulations are run to verify the robustness of this solution and determine its standard deviation. In each bootstrap simulation, the measured mass isotopomers are randomly perturbed and new flux values are calculated. The mean and standard deviation of each flux are computed by running multiple simulations. In our simulations, 20 perturbations were used. Because the primary goal of these simulations was searching for flux solutions, we used a low number of perturbations to facilitate rapid

prototyping and optimization. For future simulations where statistical significance of flux solutions is a primary objective, it is necessary to increase the number of perturbations (typically 500-1000).

The MFA algorithms used in NMR2Flux+ are dependent on minimizing the SSR between computationally solved fluxes and experimentally measured fluxes. Therefore it is necessary to design experiments and develop experimental techniques which can accurately measure the metabolites formed in biological systems.

2.3 Experimental techniques

A number of experimental methodologies have been developed which allow for the quantification of isotopically labeled atoms, the two most common being mass spectrometry (MS) and nuclear magnetic resonance (NMR). Although these methods provide complimentary information about cellular isotopomer distributions, the high cost and low resolution of NMR has led to an increase in popularity of MS based analysis²¹.

MS works on the principle of measuring a given molecule's mass to charge ratio, or m/z . In a mass spectrometer, a molecule first enters the ionization chamber where it is flooded with electrons and becomes ionized or charged. The ionized molecule is then accelerated through a magnetic field where its path is deflected in a manner proportional to its mass. A detector measures this path deflection with sensitivity on the order of individual molecules. This method of quantification necessitates prior separation of different types of molecules; therefore, MS instruments are typically coupled with a chromatography step.

Chromatography employs two phases: the mobile phase which contains the mixture to be separated and the stationary phase which is composed of a material through which the mobile phase passes. Depending on how strongly they are attracted to the stationary phase (their "affinity"), molecules in the mobile phase travel through at different speeds. Molecules with a lower affinity for the stationary phase will travel faster and take a shorter amount of time to "elute", or reach the end of the stationary phase. The time it takes a molecule to elute is termed the "retention time" and is specific to a single type of molecule. Mixtures in the mobile phase are always carried in a solvent to facilitate travel through the stationary phase. Occasionally, molecules with similar chemical structures

will have similar affinities for the stationary phase and molecules with similar masses could be difficult to differentiate in a mass spectrometer. By combining a chromatograph and a mass spectrometer, the overall accuracy of identification and quantification is greatly increased compared to using either technique alone.

A common chromatography method for separating chemical mixtures is column chromatography, where the stationary phase is packed in a tube. A variety of solvents can be used, either in the gas phase or liquid phase. Using a liquid mobile phase (liquid chromatography) allows for simple sample preparation, but operation and equipment maintenance costs are high. Operating with a gaseous mobile phase (gas chromatography; GC) requires more extensive sample preparation but comparatively inexpensive equipment. Additionally, liquid chromatography is more suited for high molecular weight compounds that cannot be easily volatilized. All intracellular metabolites such as amino acids and lipids are relatively small and can be derivatized and volatilized easily. For these reasons, gas chromatography is commonly used for sample separation in metabolomics and fluxomics applications²².

2.4 GC-MS Limitations

2.4.1 Conversion of measured compounds to central metabolic precursors

There are two main limitations to GC-MS analysis for metabolic modeling applications. First, central carbon metabolites are often difficult to measure because of their low abundance compared to biomass components such as amino acids and lipids. Second, mass spectrometry measures the *mass* isotopomer distribution (MID) of a given metabolite, not the isotopomer distribution. **Figure 2.2** lists all 8 isotopomers of alanine; however there are 3 isotopomers which all have “mass plus one”. Even though the relative presence of these isotopomers may indicate activity in different metabolic pathways, they are all measured together as a single $m+1$ category. Because metabolic modeling typically focuses on central carbon metabolism, it is necessary to translate the measured amino acid MIDs into central carbon metabolite isotopomer distributions. Mapping biomass “sink” metabolites onto central carbon precursors is typically done using literature and databases such as MetaCyc, however it is not always possible to directly map a sink metabolite MID onto its precursor’s isotopomer distribution. Often, MIDs of multiple sink metabolites who share partial carbon backbones with a precursor can be combined to fully resolve the precursor isotopomer distribution. For example, the metabolite oxaloacetate (OAA) is synthesized from Pyr[123] and CO₂[1]. Both precursor metabolite MIDs are convolved to produce the OAA MID, which cannot be directly measured. Applying singular value decomposition to Pyr[123] and CO₂[1] mass isotopomers deconvolves OAA mass isotopomers, allowing for quantification without direct measurement. It is often necessary to perform singular value decomposition multiple times, for example to deconvolve the CO₂[1] MID before OAA deconvolution.

2.4.2 Natural abundance correction

Another limitation of mass spectrometry is the inability to distinguish between naturally abundant heavy isotopes and those fed as part of the supplied label. The natural abundance of ^{13}C is 1.109%, meaning that on average, approximately 1 out of every 100 naturally occurring carbon atoms will be ^{13}C . If left uncorrected, natural abundance will lead to an overestimation of isotopomer abundance and an inaccurate picture of the cellular metabolic phenotype. The methodology for natural abundance correction is to apply the binomial distribution to each mass isotopomer in a set of experimental data. This distribution predicts the probability of k ^{13}C atoms in a molecule composed of n carbon atoms. The probability for each mass isotopomer is calculated using

$$\text{Pr} = \frac{n!}{k!(n-k)!} p^k (1-p)^{n-k} \quad (10)$$

where p is the elemental natural abundance and Pr is the mass isotopomer abundance. This can be repeated for every element in the compound of interest.

Other methods of natural abundance correction have been proposed. Fernandez et al. developed a method which corrects for deviations from the theoretical probability distribution based on experimental measurements of labeled and unlabeled substrates²³. In 2012, Millard et al. released a program called IsoCor which uses least squares optimization to further improve the accuracy of this experimental correction method²⁴. In addition, IsoCor also allows for the correction of different naturally abundant isotopes including nitrogen (^{15}N), oxygen (^{18}O), iron (^{57}Fe) and many others. A more comprehensive review of these methods and others was performed by Midani et al. in 2017²⁵.

Chapter 3 : History and Current State of Prostate Cancer Metabolomics Research

While prostate cancer was first described in the mid-nineteenth century, pioneering treatment methods were not developed until almost a century later, when Charles Huggins discovered the therapeutic effect of androgen deprivation²⁶. Surgical and radiotherapy techniques, which physically targeted tumor growth, followed soon after, yet failed to improve our understanding of the biological causes of and requirements for prostate cancer proliferation. A promising area in this regard is metabolomics, which studies the small molecule intermediates and products (metabolites) of intracellular biochemical reactions. When compared to other “omics” approaches including genomics and proteomics, metabolomics has a number of advantages with respect to disease profiling. Metabolite analysis can describe functional alterations in metabolic pathways between healthy cells and tumors which represent the summation of changes to gene expression, enzyme activity and biochemical reactions without requiring direct measurement of genomic or proteomic activity. Additionally, the total number of metabolites in any biological system is much smaller than the corresponding number of genes and proteins, which enables the construction of more complete predictive models from less data²⁷.

The majority of published studies utilizing metabolomics have focused on profiling specific metabolites of interest in order to identify “biomarkers” which can help detect and stratify the wide range of prostate cancer modalities. Sreekumar et al. profiled over 1,100 metabolite candidates by measuring relative concentrations between benign adjacent prostate ($n = 16$), clinically localized prostate cancer ($n = 12$) and metastatic prostate

cancer ($n = 14$) patients²⁸. Using a combination of liquid and gas chromatography based mass spectrometry, they identified six metabolites which increased along with prostate cancer progression: sarcosine, leucine, proline, uracil, kynurenine and glycerol-3-phosphate. In particular, sarcosine exhibited drastic increases from benign to cancerous tissue. 79% of metastatic patients and 42% of localized patients had significantly increased levels of sarcosine. No sarcosine was measured in any benign tissue sample, meaning that monitoring sarcosine levels may give insight into cancer progression and aggressiveness. Sarcosine levels in urine were also compared and while not as strongly correlated as in tissue, still allowed for the identification of prostate cancer. This initially exciting discovery was challenged by Jentzmik et al. who found sarcosine concentration in urine to be a poor indicator of prostate cancer²⁹. Even though both groups used similar analytical techniques, their methodologies and biomarker assays varied greatly. Sreekumar et al. examined the log₂ ratio of sarcosine to alanine in urine sediment while Jentzmik et al. used sarcosine levels in urine supernatant normalized to creatinine. The need for assay standardization is necessary to properly validate current reports. Regardless, the inability to reliably detect sarcosine in urine or other accessible body fluids limits its usefulness as a biomarker.

Another study used high-resolution magic angle spinning spectroscopy to quantify lactate and alanine in benign and cancerous prostate tissue samples³⁰. They found lactate and alanine concentrations to be significantly higher in biopsy tissue containing as little as 5% cancerous tissue by weight. These results imply increased glycolytic activity but are subject to variability depending on the concentration of malignant tissue in the biopsy and the severity of the cancer. van Asten et al. hypothesized that the ratio of lactate

to alanine may be a better indicator of cancer progression than measurements of both metabolites independently³¹.

Other work has been conducted examining signs of metastasis in bones using mass spectrometry methods similar to Sreekumar et al. In one study, bone biopsies were collected from 14 patients (7 localized and 7 castration-resistant cases) and compared with normal adjacent bone tissue by profiling a panel of metabolites. The largest variation was that of cholesterol, observed to be significantly higher in metastasis compared to normal bone ($P = 0.001$)³². Reasons for increased cholesterol levels include higher uptake via low-density lipoprotein receptor (LDL-R) and upregulated *de novo* synthesis from ACoA. Bone metastases were immunostained for LDL-R and a rate-limiting enzyme involved in *de novo* synthesis. All cases showed strong staining of LDL-R while rate-limiting enzyme staining was more heterogeneous. No relation between staining heterogeneity and corresponding cholesterol levels was found. Limitations of this study are evident through the concerning result that no changes in citrate levels were observed between benign and cancerous samples. This goes directly against overwhelming evidence for large changes in citrate accumulation between benign and malignant phenotypes¹¹.

A long identified feature of cancer metabolism is the deregulation of the polyamine pathway, which plays a role in the regulation of gene expression. This pathway is connected to the urea cycle via ornithine, which is decarboxylated to form putrescine, the first polyamine. Putrescine is further converted to spermidine and then spermine. Polyamines are particularly important for prostate cells as they are a major component of semen³³. A 2015 study utilizing gas chromatography-mass spectrometry (GC-MS) and

liquid chromatography-MS/MS aimed to correlate polyamine and other metabolite changes with the translocation of transmembrane protease serine 2 (TMPRSS2) to the ERG (ETS [erythroblast transformation-specific] Related Gene) oncogene³⁴. A “metabolic fingerprint” was constructed using over 55 metabolites with statistically significant variations between patients with and without the TMPRSS2-ERG translocation. Interestingly, two of the polyamines, putrescine and spermine, were decreased while spermidine, the intermediate metabolite, was increased. Consideration of confounding factors in these fingerprinting studies is critical, most notably the genetic and environmental variations between individuals from which samples are collected and analyzed. Biomarkers must be validated using appropriate experiment design to account for these variables³⁵. This discrepancy in polyamine concentrations, however, highlights an even more important and inherent limitation of high-throughput metabolic profiling experiments: the inability to contextualize changes of individual metabolites within the overall shift from benign to malignant phenotypes.

A necessary step beyond biomarker analysis is the elucidation of tumor proliferation mechanisms and the biological roles of metabolites within them. Mechanistic understanding requires knowledge of synthesis and degradation pathways, the metabolic connections between them and relative carbon flux through them. This information can only be extracted using multi-level analyses that use ‘omics’ data to inform targeted studies based on techniques such as isotope-assisted MFA³⁶. Recent advances in data processing and metabolite identification have enabled the creation of more complex and holistic methodologies which integrate multiple analytical approaches to improve phenotype characterization (**Figure 3.1**).

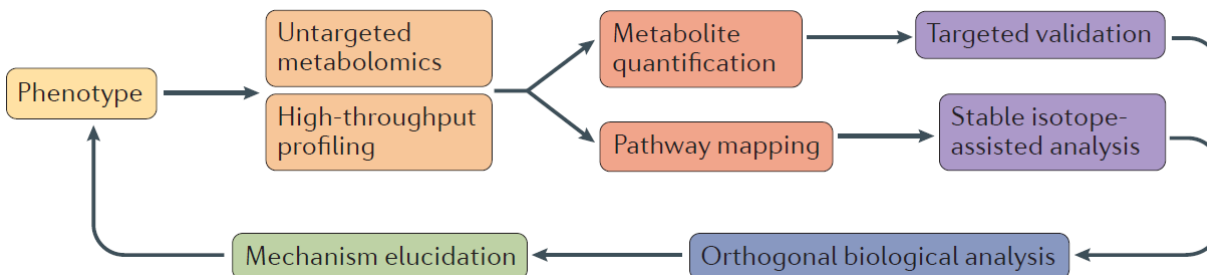


Figure 3.1 General workflow for metabolic phenotype mapping. This approach incorporates orthogonal approaches which use successive steps to build on previously gained knowledge. Reproduced with permission from Johnson et al.³⁶

One such multi-disciplinary study examined polyamine metabolism in colon cancer specifically its role in bacterial biofilm synthesis³⁷. Untargeted metabolomics strategies were first used to correlate N^1 , N^{12} -diacetylspermine (DAS) with both colon cancer and biofilm presence. This was confirmed by targeted validation as well as nanostructure-imaging mass spectrometry which showed elevated DAS levels in areas of the colon with higher biofilm concentration. Isotope-assisted metabolomics was used to track the metabolic fate of DAS by feeding colon cancer cell lines with a mixture of [U- ^{14}N]- and [U- ^{15}N]-DAS. The isotopically-labeled DAS was taken up by the cells but no concentration change was detected after 24 hours, indicating that DAS is indeed an endpoint of polyamine metabolism and a potential building block for bacterial biofilms. Increased biofilm presence was previously correlated with inflammation and a pro-carcinogenic state, even when measured in normal colon tissue³⁸. Results from these studies collectively link polyamine metabolism to colon tumorigenesis via biofilm production. These results may also have an impact on prostate cancer, as a recent study found evidence of a link between biofilms and prostate calcifications, which cause inflammation and an increased risk of tumorigenesis³⁹. The multi-level analyses and advanced

metabolomics techniques used in³⁷ yielded a more fundamental understanding of the role of polyamine metabolism within cancer proliferation mechanisms when compared to basic biomarker identification studies.

Integration of isotope-assisted MFA into prostate cancer studies is rare due to the relative infancy of the technology and the difficulty of obtaining tumor samples from patients. The most common alternatives are immortalized prostate cancer cell lines as well as *in vivo* animal models. A number of cell lines have been isolated that mimic both early state androgen dependent and late stage castration resistant tumors. The three most common cell lines are LNCaP, PC3 and DU-145. LNCaP cells are considered to represent early stage prostate cancer due to their androgen sensitive cell growth and eventual transition to androgen insensitive growth⁴⁰.

One of the earliest applications of stable isotopes used Fourier transform ion cyclotron resonance (FTICR) to measure mass differences in peptides from prostate cancer cell lines being fed naturally abundant and ¹³C-labeled arginine and lysine⁴¹. After isolated proteins were separated using SDS-PAGE and eluted peptides were measured with FTICR, the data was translated into a quantifiable spectra of proteins containing arginine and lysine. This data set augmented previous proteomic work by identifying and quantifying almost 1400 proteins, one of the largest proteomic studies to date. Accurate quantification allowed for comparison of protein expression in low and high metastatic conditions, giving a better picture of how the prostate cell proteome changes as cancer progresses.

A number of studies have explored the effects of potential therapeutic drugs on prostate cancer metabolism, typically with the goal of gaining mechanistic understanding

in order to better inform treatment strategies. The anti-diabetic drug metformin has been reported to lower cancer rates among diabetic patients when compared to other glucose control strategies⁴². To study this effect, Fendt et al. cultured three prostate cancer cell lines (LNCaP, DU-145, PC3) in the presence of varying metformin doses and either ¹³C glucose or ¹³C glutamine, as well as a control with no metformin⁴³. A key finding was the dependence of glutamine anaplerosis on metformin sensitivity. Small molecule inhibitors 968 and BPTES were used to limit glutaminase activity, which prevents the conversion of glutamine to glutamate and limits the anaplerotic capabilities of glutamine. Under these conditions, metformin sensitivity was greatly increased across all cell lines and cell numbers decreased compared to uninhibited glutaminase. Conversely, an increase in anaplerotic glutamine flux counteracted the antiproliferative effects of metformin. These findings support the hypothesis that glutamine can replace glucose as a cellular energy and carbon source. *In vitro* findings were confirmed using the *in vivo* transgenic adenocarcinoma of mouse prostate (TRAMP) mouse model. The observed therapeutic effect of metformin was limited when cells were cultured under hypoxia, with LNCaP cells showing reduced sensitivity and PC3 cells showing no sensitivity. This decrease in effectiveness is likely due to a limited dependence on oxidative glucose metabolism when oxygen is not readily available. The hypoxic condition is particularly important with respect to cancer, as most tumors have an underdeveloped network of blood vessels which limits the amount of supplied oxygen.

The condition of hypoxia was further explored by Metallo et al. using several cancer cell lines including lung, mammary, colon and squamous cell carcinoma⁴⁴. ILEs were conducted on cell lines using [1-¹³C]-glutamine to measure downstream

incorporation of glutamine carbon in the TCA cycle and [5-¹³C]-glutamine to measure reductive flux in the glutaminolysis pathway and its contribution to lipogenic ACoA pools. Under normoxia, glucose oxidation contributed approximately 80% of lipogenic ACoA and glutamine reduction contributed 20%. Under hypoxia the primary carbon source changed, with glutamine reduction contributing 80% of the carbon necessary for lipogenesis. Additionally, it was found that hypoxic cells are more dependent on glutamine and proliferated approximately half as fast as normoxic cells when growth rates were compared in a glutamine deficient condition.

To study the mechanisms driving the shift to a reliance on reductive glutamine metabolism, ILEs were conducted using [U-¹³C]-glucose as a tracer for TCA cycle metabolites. A significant decrease in flux through the pyruvate dehydrogenase (PDH) complex was observed as well as the depletion of the citrate pool, likely to supply carbon to reductive carboxylation pathways. PDH activity under hypoxia was partially restored using the PDH promoter dichloroacetate, indicating a potential therapeutic target which may limit glutamine reduction under hypoxia. These ILEs provided insight into the phenotypic shift of cancer cells from normoxia to hypoxia. Although not directly applicable to prostate cancer, the presented methodologies are an excellent reference to help guide the acquisition and analysis of prostate cancer data.

Recently, there has been research into the effects of melatonin on prostate cancer metabolism. Historically, melatonin has been known to regulate sleep patterns; this is partially achieved through the suppression of glucose metabolism at a cellular level. Hevia et al. used LNCaP and PC3 cell lines to test this effect on prostate cancer by feeding labeled 2-deoxy-D-[1-³H]-glucose⁴⁵. Both cell lines exhibited lower glucose uptake,

however the effect was more pronounced in the early stage LNCaP cells. Further experiments were conducted using U-¹³C glucose to link decreased glucose consumption to altered synthesis pathways for essential downstream metabolites. Lactate production was reduced by almost 50% while TCA cycle metabolites were reduced by approximately 15% in LNCaP cells. No changes in TCA cycle metabolites were observed in PC3 cells, indicating negligible effects on later stage phenotypes. These results support a phenotypic shift and decreased melatonin efficacy in androgen insensitive prostate cancer. The proposed mechanism of action links melatonin to the downregulation of glucose transporters, which may only be important for glucose-dependent cells. Though results are not entirely negative, the observed heterogeneity of prostate cancer metabolism limits the effectiveness of melatonin at halting proliferation.

The majority of metabolomics and fluxomics research on prostate cancer has been conducted on immortalized cell lines given the difficulty and complexity of *in vivo* studies. Recent advances in imaging technology using nuclear spin hyperpolarization of ¹³C labeled substrates have enabled high resolution temporal and spatial profiling of cancer metabolism in both *in vivo* models and diagnosed patients⁴⁶. Hyperpolarized metabolites offer at least a 10⁴-fold increase in detection sensitivity compared to standard isotopically labeled substrates, overcoming the largest hurdle in clinical magnetic resonance spectroscopy. The first in-human fluxomics study used hyperpolarized 1-¹³C pyruvate to examine lactate dehydrogenase activity in prostate cancer patients by tracking 1-¹³C lactate appearance over time⁴⁷. 31 patients were injected with a solution containing hyperpolarized 1-¹³C pyruvate and tumors were scanned in five second intervals post injection using magnetic resonance imaging. Resulting images gave insight into both the

rate of lactate appearance as well as the locations of production within the tumor. Surrounding benign tissue was also imaged to compare concentrations to the tumor. This proof of concept study validated the feasibility of using hyperpolarized isotopes for in-human imaging and confirmed a number of results from previous studies on mouse models. Pyruvate uptake was observed 20 seconds after injection and the 1-¹³C pyruvate/1-¹³C lactate ratio in malignant tissue was elevated compared to normal tissue. Observing the compartmentalization of lactate production also proved useful, as one patient was diagnosed with a bilateral tumor separated by a central benign gland. This morphology was not observed in more conventional imaging techniques and had to be confirmed with a biopsy. The ability to detect and stratify tumors using non-invasive imaging techniques is especially important to prostate cancer due to its heterogeneity compared with other forms of cancer.

The main technical limitation of this technique is the short time before the hyperpolarization of the substrate decays, termed “relaxation time”. 1-¹³C pyruvate has a relaxation time of approximately 60 seconds and the substrate must be prepared, filtered, verified and delivered to the patient in a sterile environment.

While it is considerably more expensive, labor intensive and complex, conducting research using *in vivo* human models as opposed to *in vitro* or computational models is critically important to accounting for the vast number of factors which influence cancer proliferation. This work employs a mixture of approaches and we hope lays the foundation for future *in vivo* metabolomics research.

Chapter 4 : Methods, Results and Discussion

4.1 Methods

4.1.1 Prostate cancer cell line culture and isotope labeling

In order to study the malignant phenotype, we first performed experiments on the LNCaP prostate cancer cell line under four conditions which included the LNCaP control, LNCaP treated with dihydrotestosterone (DHT), LNCaP treated with MDV3100 (an androgen receptor inhibitor) and CSS90 (LNCaP subline evolved to be androgen insensitive). Our collaborators at the University of Maryland, Baltimore cultured LNCaP cells under these four conditions in Roswell Park Memorial Institute (RPMI) 1640 medium containing 4.5 g/L of 50% U-¹³C glucose. In addition to labeled glucose, unlabeled glucose was present at a concentration of 2 g/L. Unlabeled amino acids were also present at the following concentrations: Gln- 300 mg/L, Arg- 200 mg/L, Asn, Cys, Leu, Ile- 50 mg/L, Lys- 40 mg/L, Ser- 30 mg/L, Asp, Glu, Pro, Thr, Tyr, Val- 20 mg/L, His, Met, Phe 15 mg/L, Gly- 10 mg/L, Trp- 5 mg/L. Under each condition, cell metabolism was quenched at 24 hours and 48 hours after addition of labeled glucose and frozen cells were sent to the Metabolic Engineering Laboratory for processing.

4.1.2 Soluble metabolite extraction

Cell suspensions were centrifuged at 8000 rpm and 25 °C for 10 minutes. The supernatant was removed using a 25 mL serological pipet until approximately 2 mL remained. A 2 mL serological pipet was used to resuspend the cell pellet in the remaining medium. Resuspended cells were transferred to a 2 mL centrifuge tube and centrifuged at 13,000 rpm and 25 °C for 5 minutes. The supernatant was decanted using a 200 µL pipet and discarded. 700 µL of methanol and 25 µL of deionized (DI) water was added to

the cell pellets, which were then vortexed for 1 minute. 370 μL of chloroform and an additional 700 μL of DI water was added to the cell pellets for a total volume of approximately 1.8 mL. Cell pellets were then centrifuged at 13,000 rpm and 25 $^{\circ}\text{C}$ for 5 minutes. After centrifugation, each tube contained three separate layers: an aqueous layer on top (contains free amino acids, sugars and other central carbon metabolites), a pellet layer in the middle (contains proteins and other components of biomass) and an organic layer on the bottom (contains lipids and sterols). The top layer (aqueous) and bottom layer (organic) were decanted using a Pasteur pipet and transferred to new 2 mL centrifuge tubes, leaving the cell pellet in the original tube. The tubes containing the organic layer and cell pellet were frozen at -80 $^{\circ}\text{C}$. The aqueous layer was dried overnight using nitrogen gas. The next day, metabolites in the dried tubes were resuspended in 150 μL of DI water and transferred to a 300 μL gas chromatograph (GC) vial. All vials were lyophilized overnight to completely remove water. After lyophilization, 50 μL of anhydrous dimethylformamide (DMF) and 25 μL of 20 mg/mL methoxyamine hydrochloride in pyridine were added to each GC vial. All vials were vortexed for 1 minute to dissolve all dried metabolites. The vials were then heated on a heating block at 35 $^{\circ}\text{C}$ for 90 minutes to promote methoxyamination. 25 μL of MTBSTFA + 1% TBDMCS (*N-tert*-butyldimethylsilyl-*N*-methyltrifluoroacetamide with 1% *tert*-butyldimethylchlorosilane) was added to all vials, which were then heated on a heating block at 75 $^{\circ}\text{C}$ for 90 minutes. Derivatized samples were injected into a GC-MS with DMF as the solvent.

4.1.3 Quantification of mass isotopomers by GC-MS

We analyzed all samples using a Varian 300-MS quadrupole GC-MS. Each sample was injected in three technical replicates at a split ratio of 1:15 between the sample and helium, the carrier gas. We collected mass spectra for 40 minutes using the selected ion monitoring mode. Using the Varian MS Workstation software, we isolated each raw metabolite peak and converted the data to a comma-separated value file.

We processed raw peak data with a MATLAB program which uses singular value decomposition to deconvolve mass contributions to MIDs from fed isotope labels and less common naturally abundant isotopes. The MATLAB program corrects for naturally abundant isotopes of each atom in the molecule as well as atoms added from the derivatization process such as silicon.

Although we collect mass spectra for most amino acids, labeling data is only useful for nonessential amino acids, which are synthesized *in vivo*. If essential amino acids are present, they originated in the fed medium and cannot become labeled as they are not synthesized through metabolic pathways. The essential amino acids are His, Ile, Leu, Lys, Met, Phe, Thr, Trp and Val. The raw peak data from these amino acids is not processed.

4.2 Results and Discussion

4.2.1 Prostate cancer cell line data and stationary estimation

We acquired enrichment data from six metabolites across the four conditions and two time points; enrichment data for the LNCaP condition is shown in **Figure 4.1**.

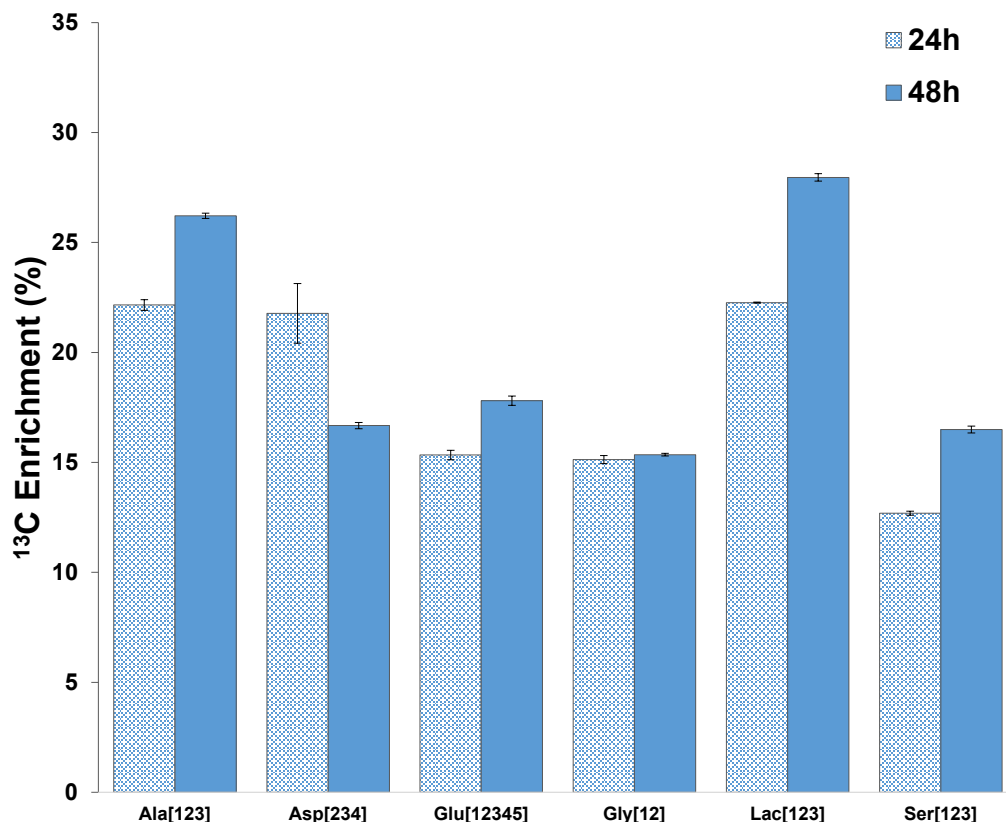


Figure 4.1 Enrichment data after 24 hour and 48 hour exposure to ^{13}C medium. Bracketed numbers indicate each carbon molecule in the measured fragment. Error bars show the standard deviation in each measurement across biological replicates. Enrichment is calculated from the measured MID of each metabolite and is represented as a percentage of total carbon in a specific metabolite pool.

Using isotopomer abundance data, we identified statistically significant isotopomer differences across all four experimental conditions and both measured time points (**Figure 4.2**). Within the isotopomer solution space, a difference of >0.06 is very significant

and can correspond to drastically different metabolic phenotypes. The total number of different (>0.06) isotopomers was not consistent across time points; of the six condition comparisons only one, CSS90-DHT, retained a similar number of isotopomer differences between 24 and 48 hours. At the 48 hour time point, the CSS90-MDV comparison showed the largest disparity, with almost 30% of isotopomers measured as significantly different. Large changes in the DHT-MDV, LNCaP-DHT, LNCaP-MDV and LNCaP-CSS90 comparisons between the 24 hour and 48 hour time points indicate that during the approach to isotopic steady state, the relative rates of carbon metabolism under each condition were different.

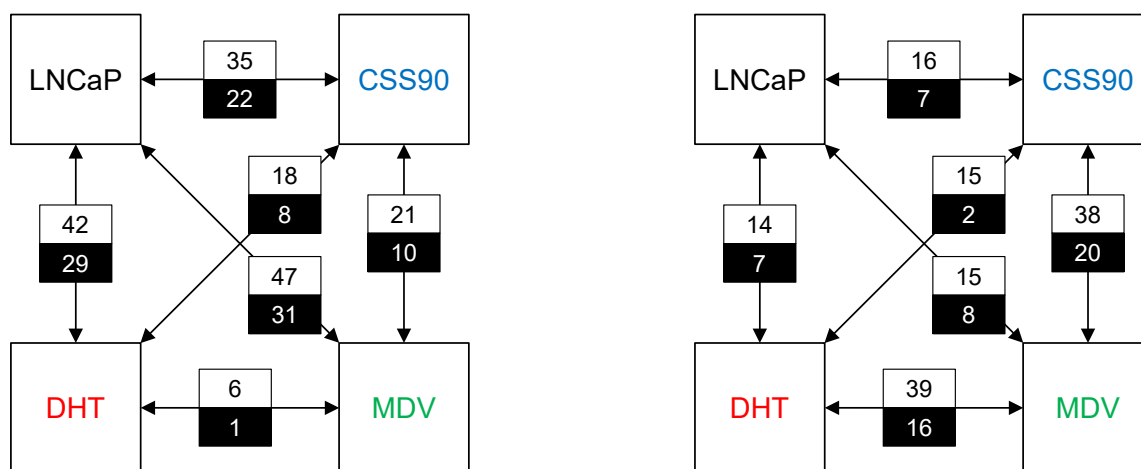


Figure 4.2 Comparison of isotopomer abundance data. The number of reported isotopomer differences was determined using a Student's t-test evaluating differences of >0.03 (white boxes) and >0.06 (black boxes), both with a p -value < 0.05 . Conditions were compared at the 24 hour (left) and 48 hour (right) time points. In total, 69 isotopomer comparisons were made for each condition comparison at each time point.

All measured metabolites did not reach isotopic steady state by the 24 hour time point. **Figure 4.1** shows the increase in labeling between the 24 hour and 48 hour time points in the LNCaP condition. Similar trends were observed in all other conditions. Because isotopic steady state is required for NMR2Flux+ MFA simulations, we used nonlinear optimization techniques to estimate the steady state mass isotopomer

distribution of each metabolite fragment. Three main assumptions were used to perform nonlinear optimization. First, the observed isotopomer abundances were a superimposition of ^{13}C -labeled isotopomers synthesized *de novo* by the cells and the naturally abundant isotopomers present in the cells before the labeled experiment. Second, the initially present material gets washed out with time, so that at infinite time or isotopic steady state, we will obtain the true isotopomer distribution corresponding to the *de novo* isotopomers. Third, the incorporation of ^{13}C label can be estimated using the following equation:

$$I(t) = (I_{\infty} - I_0)(1 - e^{-t/\tau}) + I_0 \quad (11)$$

where I is the ^{13}C enrichment, I_{∞} is the stationary enrichment, I_0 is the initial enrichment and τ is the characteristic time constant for the rate of incorporation of ^{13}C label into a given metabolite fragment. We used the generalized reduced gradient algorithm to fit experimental data by varying the time constant τ to minimize the squared error between experimental isotopomer abundance and abundance calculated using **Equation 11**, which was derived using principles in van Winden, et al.⁴⁸. The values of I_{∞} corresponding to minimized squared error for each metabolite fragment were used in NMR2Flux+ for MFA. Because the generalized reduced gradient algorithm achieves local convergence only, we used the first assumption to discard solutions where I_{∞} varied greatly from the 48 hour time point. **Figure 4.3** shows the fit between the measured abundances and calculated abundances for a few of the metabolite fragments. Most fitted abundances matched well with the measured values and the average χ^2 error across all metabolite fragments for a given condition was 0.083 (**Figure 4.4**).

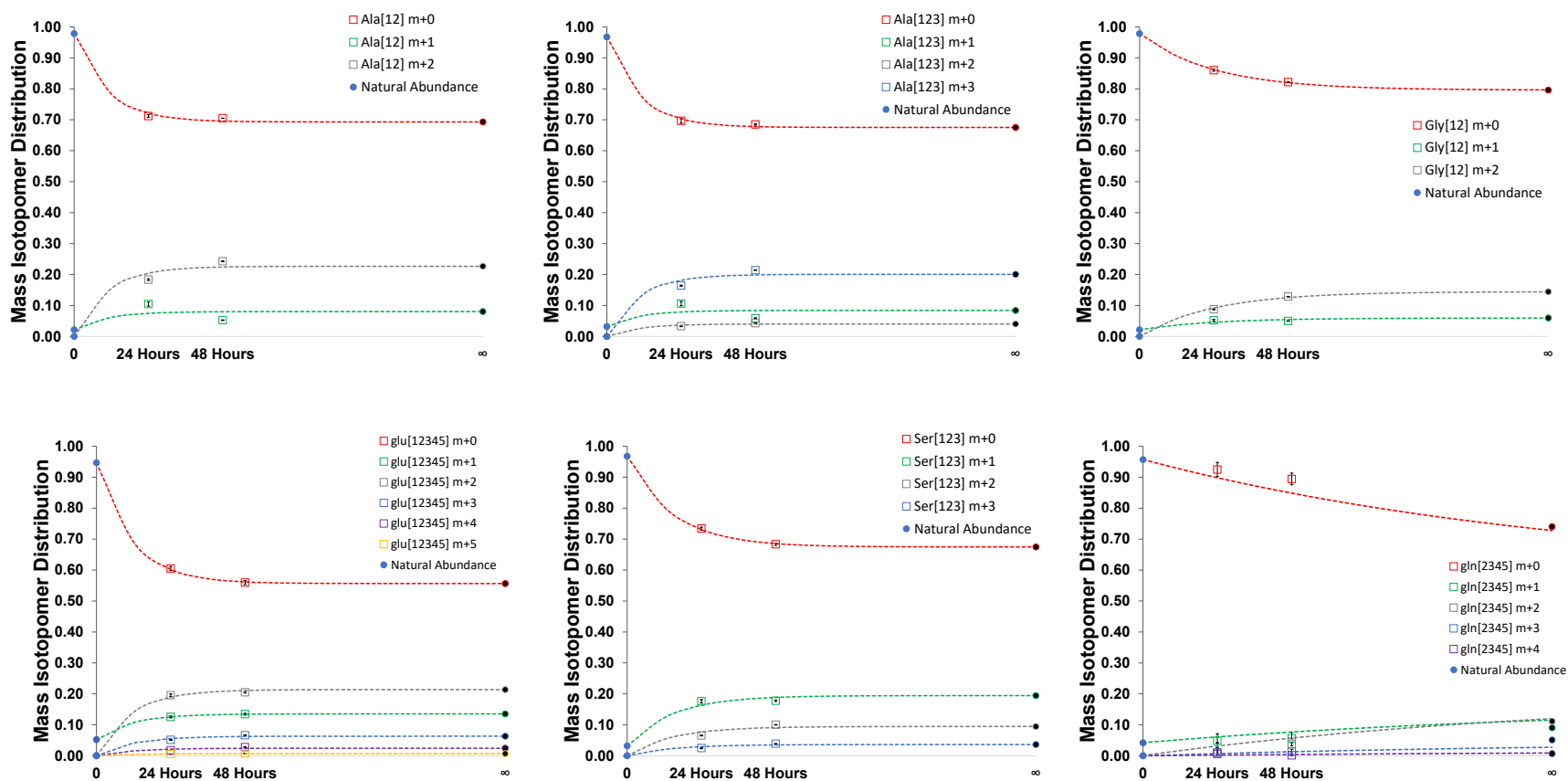


Figure 4.3 Estimation of stationary enrichment for six metabolite fragments. Fitted results are presented for Ala[12], Ala[123], Gly[12], Glu[12345], Ser[123] and Gln[2345]. All fragment measurements were taken from the LNCaP condition. Natural abundance is represented by the blue circles and estimated using the binomial expansion method presented in Chapter 2 of this work. Dotted lines represent the curve fitted using the experimental data (squares). Black circles are the estimated enrichment at isotopic steady state, represented by the infinite time point in the model

We observed less effective fitting for some metabolite fragments like Gln[2345] (see **Figure 4.3**). In this case, Gln labeling was similar across both time points which caused the fitted time constant to be much larger than most metabolites. The steady state MID was much different than the 48 hour MID, indicating an ineffective fit. As a consequence, Gln was not included in NMR2Flux+ simulations.

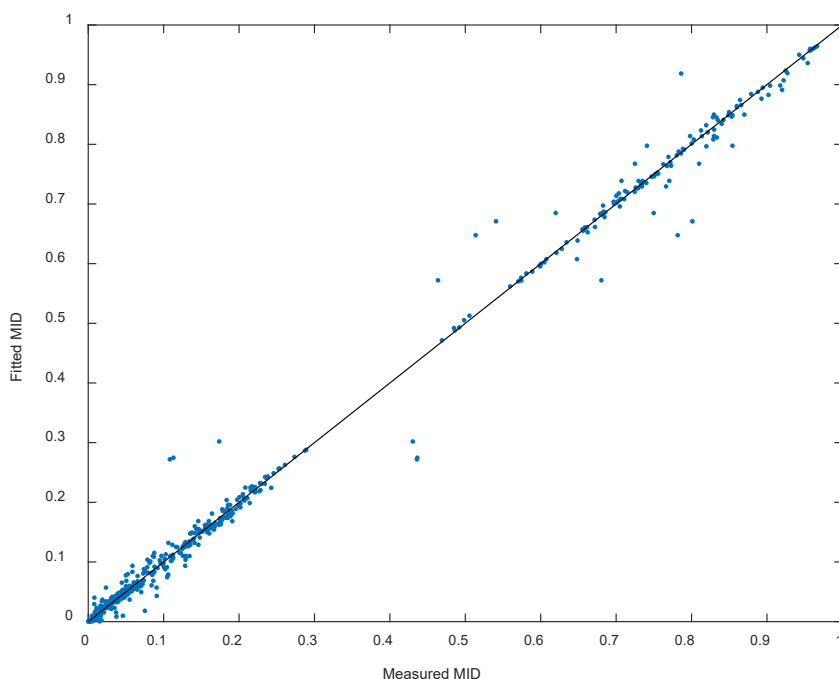


Figure 4.4 Parity plot of fitted mass isotopomer abundances vs. measured abundances. The y-axis corresponds to the fitted mass isotopomer abundances used in NMR2Flux+ simulations. The x-axis corresponds to the measured mass isotopomer abundances at each time point. The $y=x$ line represents a perfect match between measured data (input) and fitted data (output).

To verify the accuracy of fitted values, we compared τ values for different metabolite fragments of the same metabolite, which are expected to have similar time constants. All time constants showed little variance across metabolite fragments from the same metabolite and condition, giving further confidence in fitted values (**Figure 4.5**). A full list of fitted abundances is available in the supplementary material file, S2.

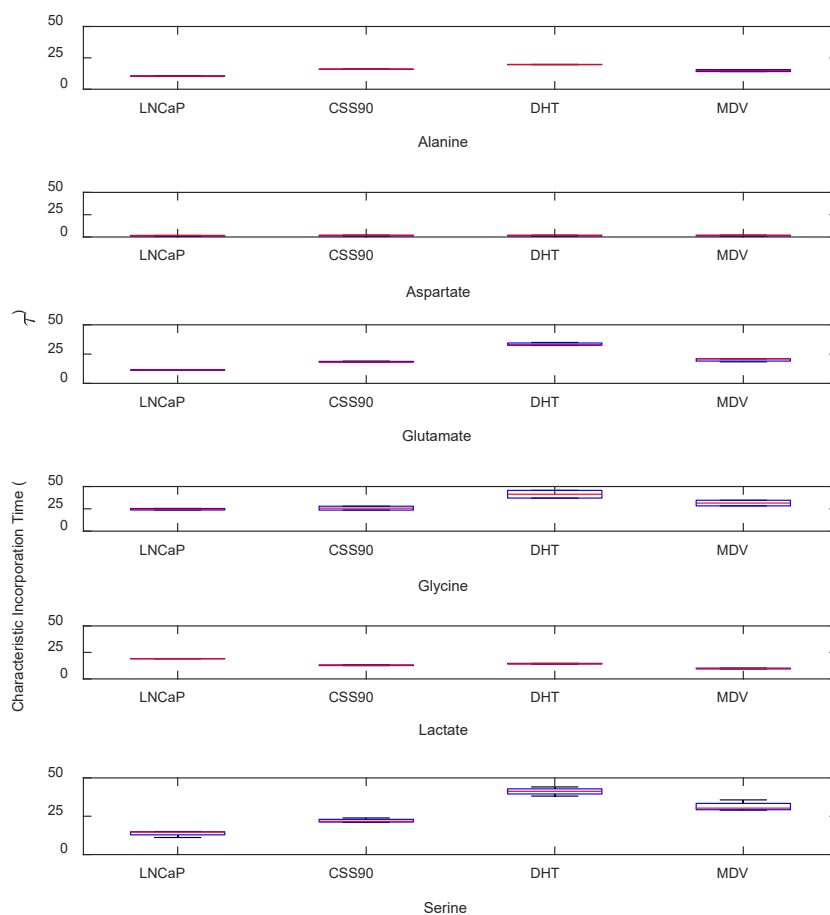


Figure 4.5 Box and whisker plot of fitted values for the time constant, τ . Data for each box comes from a single metabolite from a single condition. Each data point used to construct the box is a value of τ from each measured fragment from the metabolite. For example, Alanine fragments into two measurable fragments with m/z of 232 and 260, respectively. Each alanine box is generated from the τ value for these two fragments. Metabolites with more fragments contain more data points per condition.

4.2.2 NMR2Flux+ simulation of central carbon metabolism

We used the fitted stationary MIDs for measured metabolites to estimate the net fluxes of central carbon metabolism in prostate cancer cells. Glycolysis and the pentose phosphate pathway were incorporated into **Model 1 (Figure 4.6)**. This simple model served as a starting point for flux estimation and additional models were created by adding to this model. The global SSR values were 125 for LNCaP cells, 111 for CSS90 cells, 122 for MDV treated cells and 117 for DHT treated cells.

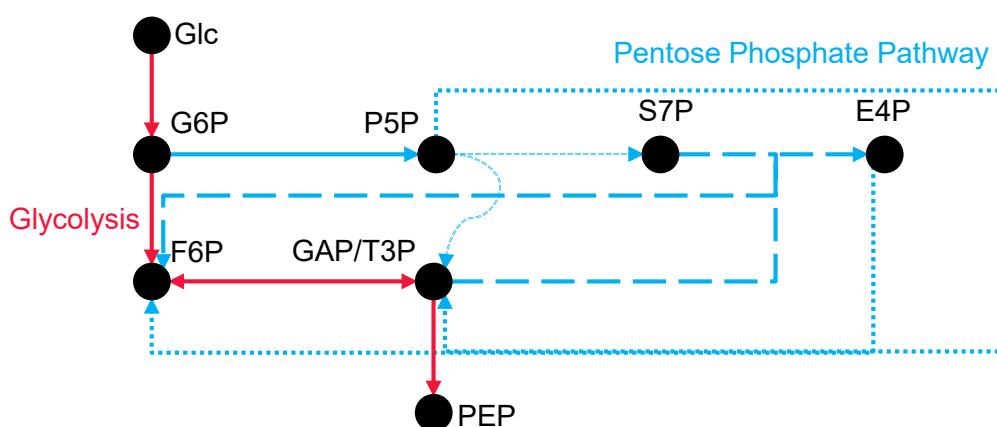


Figure 4.6 NMR2Flux+ Model 1. Each metabolite in the model is represented by a black circle and each metabolic pathway has a unique line color. The reactions comprising all pathways are represented as lines connecting the metabolites. This simple model was created as a foundation which allowed for more complex models to be built by adding to it. This eased the troubleshooting process which corrected errors present in early iterations of the model. Final SSR values for this model were 125 for LNCaP cells, 111 for CSS90 cells, 122 for MDV treated cells and 117 for DHT treated cells.

After successfully running simulations on **Model 1**, the tri-carboxylic acid cycle and the urea cycle were added to create **Model 2 (Figure 4.7 a)**. The models were primarily constructed using genomic annotation data from the HumanCyc database, a subset of information available in the larger MetaCyc database relevant to the human genome. The parameters of the experiment limited the ability to fit measured MIDs to urea cycle fluxes; therefore we removed the urea

cycle to create **Model 3 (Figure 4.7 b)**. Feeding a different carbon label (e.g. 1,2 ^{13}C) or simultaneously feeding a ^{15}N nitrogen label and a carbon label may resolve urea cycle fluxes.

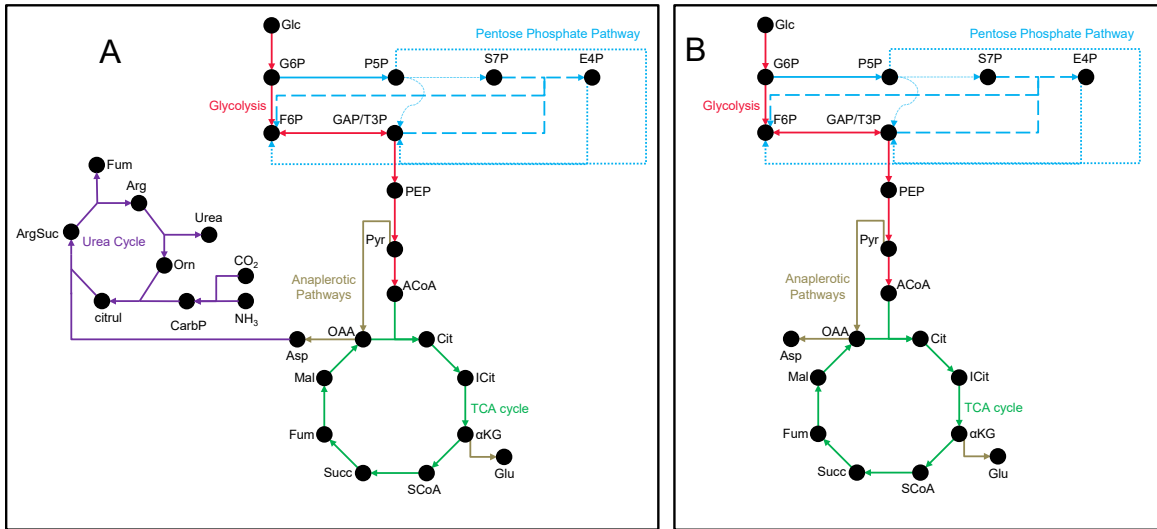


Figure 4.7 NMR2Flux+ Model 2 and Model 3. (A) Model 2 used for flux estimation from measured metabolites. Each metabolite in the model is represented by a black circle and each metabolic pathway has a unique line color. The reactions comprising all pathways are represented as lines connecting the metabolites. (B) Model 3, the final model containing glycolysis, the pentose phosphate pathway and the TCA cycle. All flux estimation data was acquired using this model.

Each model consists of six input files in CSV (comma-separated value) format, which are typically prepared in Microsoft Excel. Input file 1 lists all metabolites present in the model and the number of carbon atoms in each molecule. Most precursor metabolite isotopomer abundances are not directly measured, but inferred from their downstream products, typically amino acids. The measured amino acid MIDs are captured in input file 3. Input file 4 maps the unmeasured precursor metabolites onto the measured amino acids, allowing for flux calculation of reactions involving unmeasured metabolites. The reaction network is described in input file 2 in the form of carbon rearrangement information.

Instructions for creating input file 2 and input file 4 are shown in **Figure 4.8**. All other input files are self-explanatory.

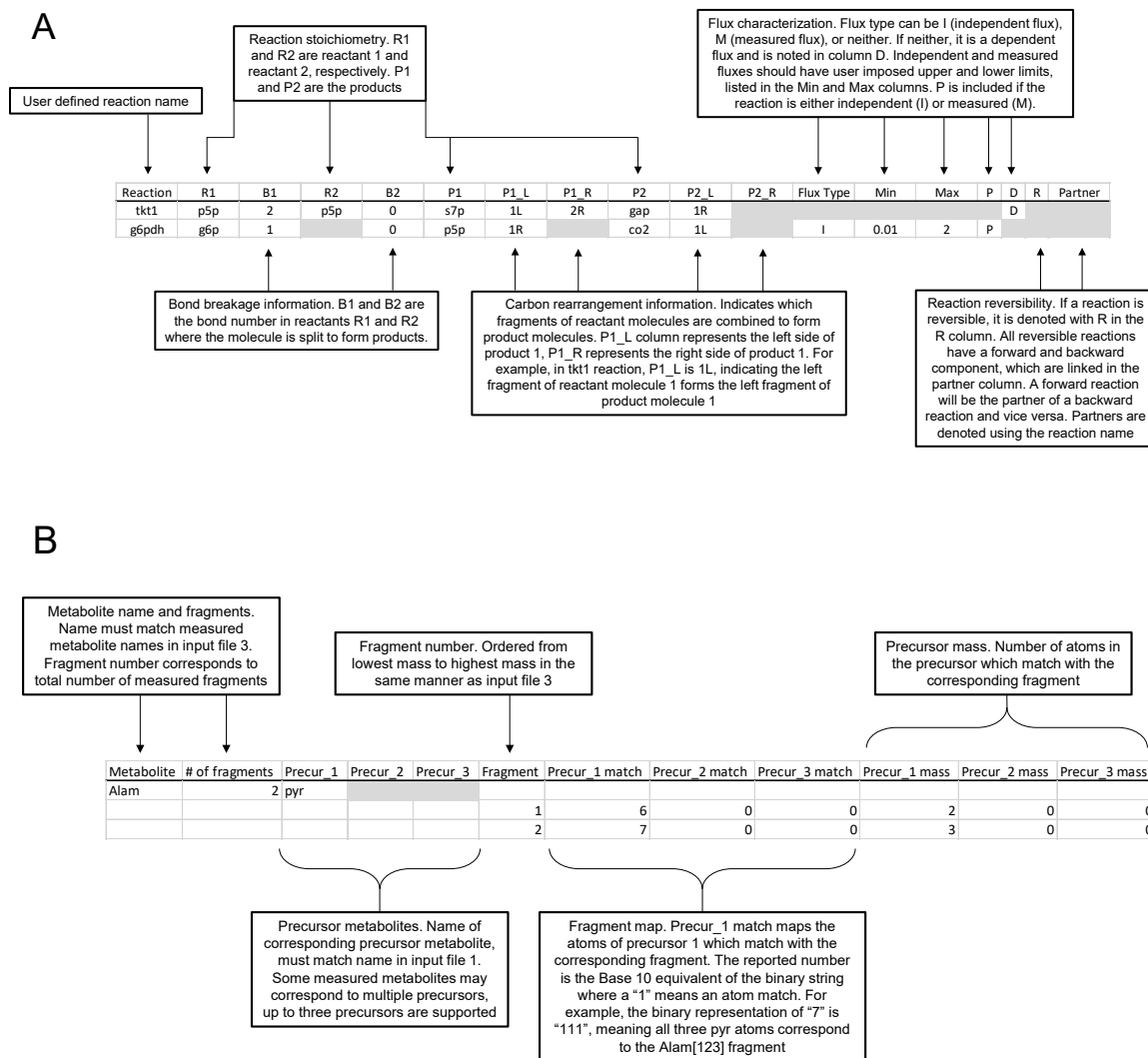


Figure 4.8 Explanations for NMR2Flux+ input file 2 and input file 4. (A) Input file 2 provides information on carbon atom rearrangement. Column headings are added for explanation but not included in the full model. Grey cells indicate empty cells. (B) Input file 4 maps precursor metabolites onto measured “sink” metabolites. Precursor names have been altered from the convention used in the full model for clarity.

Input file 5 provides information on labeled substrate fed to the network.

The substrate labeling is represented in this file using the Base 10 equivalent of the binary string where a 1 represents ^{13}C and a 0 represents ^{12}C . For example, if uniformly labeled ^{13}C glucose is fed, the identifier “63” is used in input file 5 as

the binary string representing 63 is “111111”. The final file, input file 0, is used to set simulation parameters including the number of isotopomer perturbations and the step size for the simulated annealing algorithm. All input files are available in the supplementary material, sections S4-S9.

We set the standard deviation for estimated isotopomers to 0.01 to capture inaccuracies in the MS detector and the error from stationary abundance fitting. In addition to SSR minimization, additional simulations were run with randomly perturbed isotopomers to capture the covariance between flux values and empirical measurements. We report the average flux value from these perturbations along with the standard deviation to give a confidence interval for each flux value.

In addition to computing the standard deviation for each flux value, we also used the Lilliefors normality test to verify the simulated fluxes are normally distributed. Based on the Kolmogorov–Smirnov test, it tests the null hypothesis that a dataset comes from a normally distributed population. The expected average or variance of the data is not required to test this null hypothesis. All reported flux values have been tested and confirmed to be normally distributed across all isotopomer perturbations.

The global SSR values were 462 for LNCaP cells, 389 for CSS90 cells, 455 for MDV treated cells and 357 for DHT treated cells. The SSR values were consistent across all conditions and the reported standard deviations were low enough to validate the data and the observed phenotypic differences between the conditions. The flux values simulated from isotopomer perturbations were also

confirmed to be normally distributed using the Lilliefors test. Simulated isotopomers corresponding to each flux set agreed well with fitted stationary values (**Figure 4.9**).

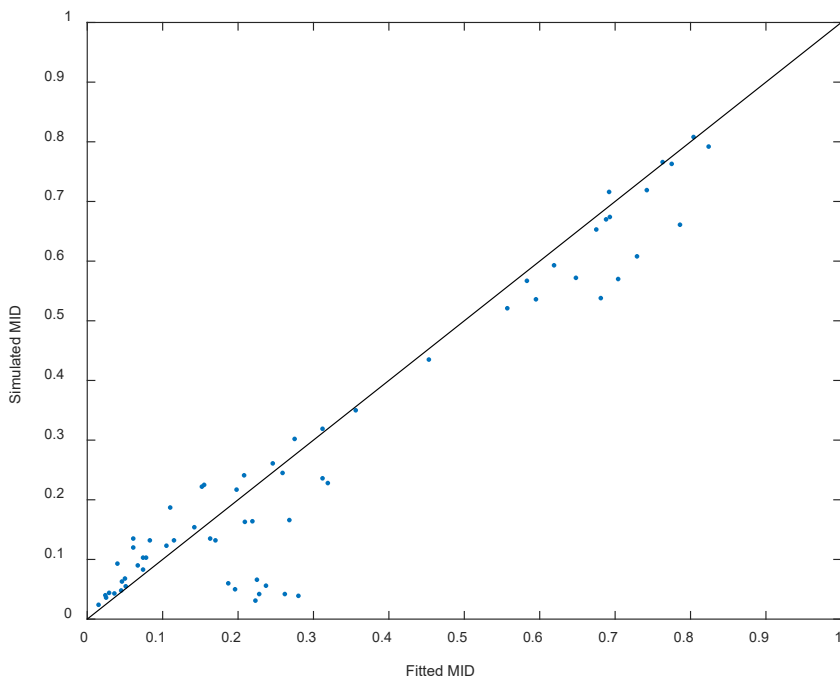


Figure 4.9 Parity plot of simulated mass isotopomer abundances vs. fitted abundances. The y-axis corresponds to the simulated mass isotopomer abundances which produced the simulated flux values. The x-axis corresponds to the fitted stationary mass isotopomer abundances, as discussed in section 4.2.1, which were used as input data for all NMR2flux+ simulations. The $y=x$ line represents a perfect match between fitted data (input) and simulated data (output).

An important branch in the central carbon metabolic model (**Figure 4.7 b**) occurs at the metabolite glucose-6-phosphate, which can either be converted to fructose-6-phosphate via glycolysis or pentose-5-phosphate via the pentose phosphate pathway (PPP). The metabolic end products of the PPP feed back into glycolysis, however the intermediates generated by the PPP are more advantageous for rapidly dividing cells due to the production of nucleotide precursors as well as the reducing agent nicotinamide adenine dinucleotide

phosphate (NADPH). Glycolysis and the PPP are closely linked and many contributing factors influence their regulation

In our model, LNCaP cells did not prefer one pathway over the other, shuttling approximately equal molar quantities of carbon through glycolysis and the PPP. When treated with MDV, $62\% \pm 25\%$ of the carbon flux went through the PPP, possibly counteracting the downregulation of androgen receptors. Interestingly, the androgen-insensitive CSS90 cell line preferred glycolysis over the PPP. This may be a consequence of androgen insensitivity and therefore a diminished reliance on supplying adequate NADPH equivalents for lipid biosynthesis. **Figure 4.10** shows the flux partition between these two pathways for all conditions. All four conditions exhibited PPP flux dramatically higher than that of normal cells, where it accounts for 5-30% of glucose metabolism depending on the tissue cells⁴⁹. This represents a clear deviation from the typical benign metabolic phenotype.

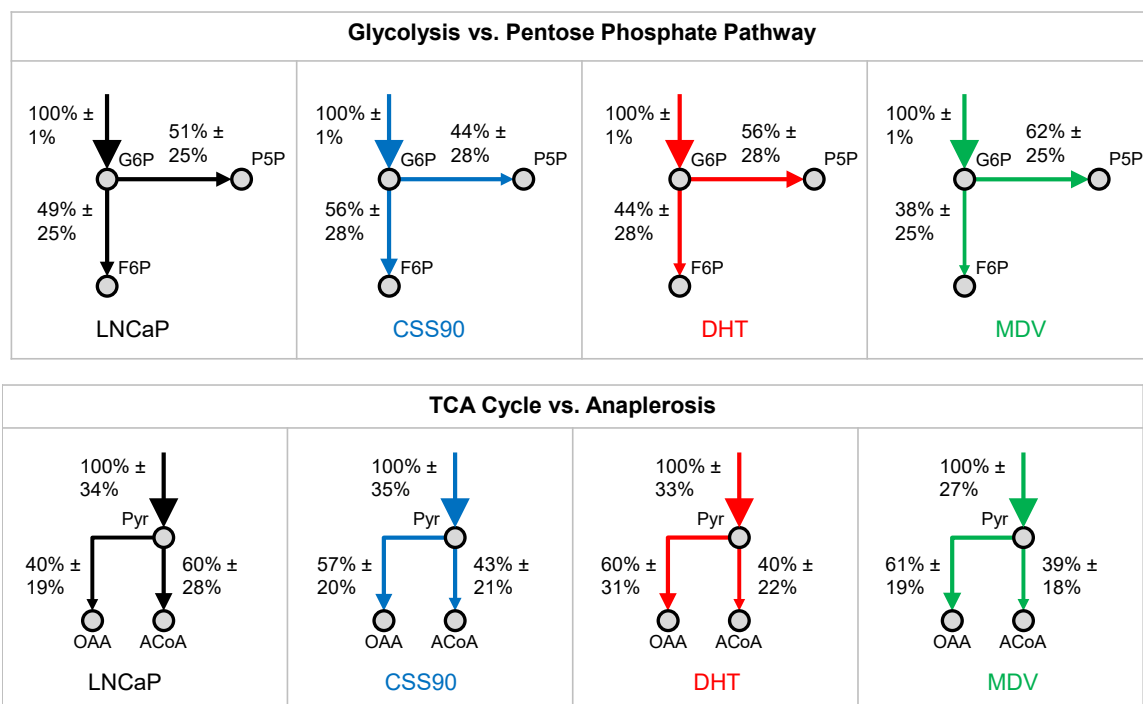


Figure 4.10 Flux partitioning at central metabolic branch points. Relative carbon flux from the catabolism of glucose through glycolysis or the pentose phosphate pathway (top) and pyruvate through the TCA cycle or anaplerosis (bottom). Arrow thickness is proportional to flux values. Flux percentages are normalized based on a 100% input flux. Error percentage in pyruvate input flux is proportional to error in simulated pyruvate flux.

The production fluxes of glutamate from α -ketoglutarate and aspartate from oxaloacetate both increased from LNCaP cells to CSS90 cells. From a basis of 100 moles of glucose entering, glutamate and aspartate fluxes were 17.5 ± 9.8 and 31.0 ± 9.9 , respectively, in LNCaP cells and 30.0 ± 9.6 and 42.3 ± 10.3 respectively in CSS90 cells. The increase was most significant in DHT treated cells, with flux values of 39.2 ± 16.2 and 54.3 ± 15.9 . The MDV-treated cell population exhibited glutamate and aspartate fluxes similar to the CSS90 cells: 31.4 ± 10.2 and 50.9 ± 10.0 respectively. These results indicate that the available pools of glutamate and aspartate are much higher in more malignant conditions and that flux is diverted away from the TCA cycle. The flux through the latter half of the TCA cycle

(succinate to oxaloacetate) was 33.5 ± 10.5 for LNCaP, 19.7 ± 7.8 for CSS90, 13.9 ± 5.2 for MDV and 22.3 ± 7.7 for DHT. This supports the conclusion that prostate cancer cells rely on glutaminolysis and lipogenesis to fuel rapid growth. Flux solutions for all cell lines are shown in **Figure 4.11** as well as in supplementary material S3.

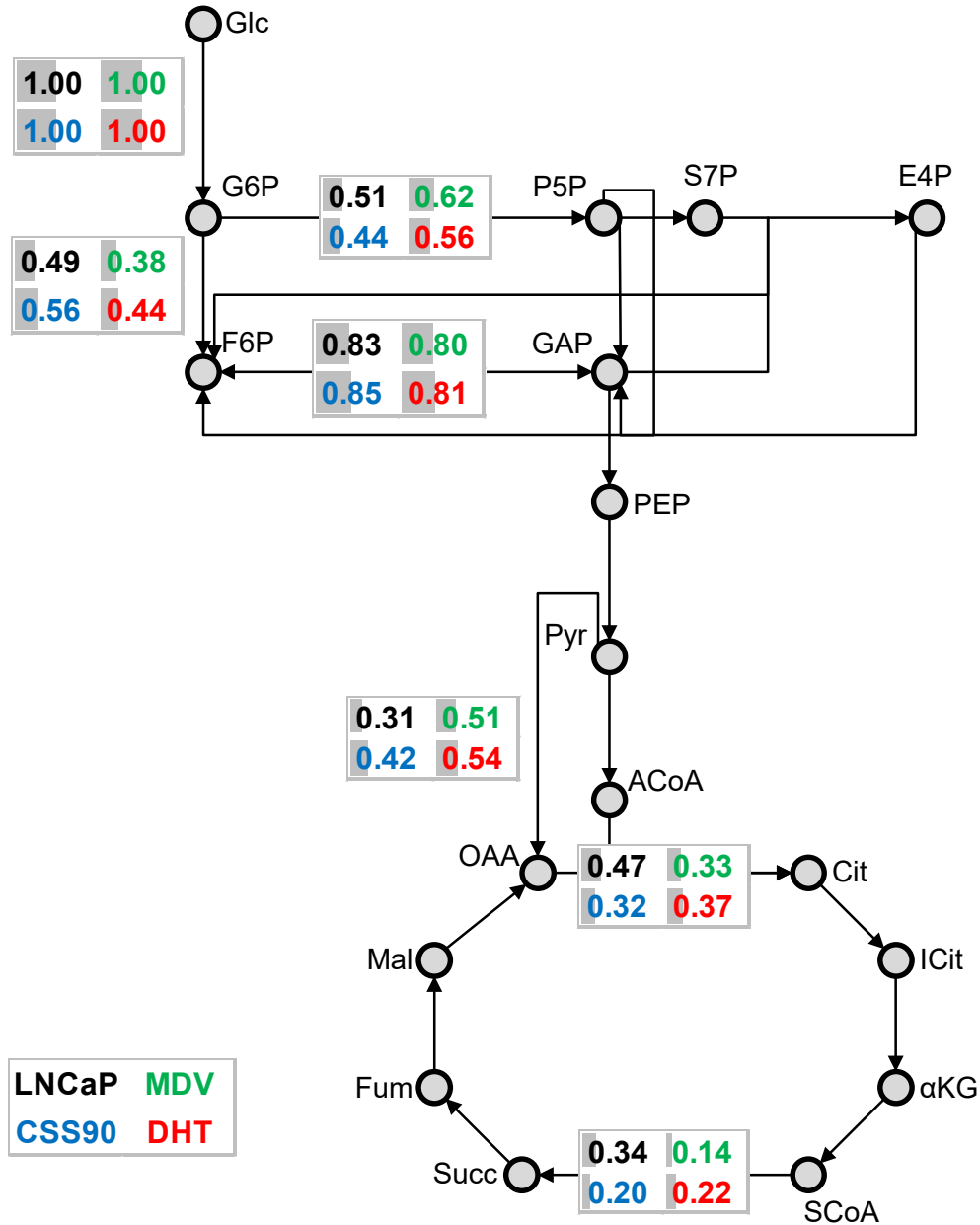


Figure 4.11 Flux solutions for all experimental conditions. Flux values for each condition are displayed next to the corresponding reaction. Grey bars overlaid below flux values represent the relative flux compared to the basis of 1 mole of glucose entering the network. A comprehensive list of flux values is available in supplementary material file S3.

The phenotype of MDV treated cells closely mirrored the more aggressive and malignant CSS90 and DHT conditions. This result is unexpected as MDV has been shown to inhibit androgen receptor signaling and decrease tumor proliferation⁵⁰. It is possible that inhibition of androgen receptors has greater

implications in other areas of metabolism such as lipid metabolism which have not been explored in this work.

There were conditions and measurements from the isotope labeling experiment which limited the resolution of obtained flux data. In all conditions, the global SSR value was above the critical value of 59.9 taken from a χ^2 distribution with degrees of freedom equal to the number of measured mass isotopomers used in the model. One cause of this high SSR is likely experimental conditions which included unaccounted carbon sources. The medium used to grow cells under all conditions contained glucose and additional unlabeled amino acid sources which were unaccounted for in the mass isotopomers used in simulations. For a cell population which is fed exclusively 50% U- ^{13}C glucose, it is expected that each metabolite will have a ^{13}C enrichment of 50% at isotopic steady state. Data from supplementary material file S1 shows that at the 48 hour time point, most metabolites had labeling of approximately 25%, with a maximum enrichment of 30% for certain metabolites. This indicates that approximately 25% of carbon participating in cellular metabolism was not captured in the measured mass isotopomers. To decrease SSR and increase flux resolution, future isotope labeling experiments should be designed to minimize the presence of unlabeled carbon sources. Additional simulation optimization strategies are discussed in **Chapter 5**.

In addition, the measured aspartate flux varied uniquely between the 24 hour and 48 hour time points, which led to a fitting error which was higher than other isotopomers used in the models. Cumulative χ^2 error for the Asp[376] fragment (LNCaP condition) was 0.09, higher than any other metabolite fragment.

With respect to χ^2 error in the model, glycine isotopomers contributed the most of any metabolite, with an average SSR of 113.5 across all conditions. Glycine is synthesized from serine, so this high SSR indicates a disagreement in serine and glycine labeling. Due to poor fitting of Gln, this metabolite was excluded from simulations. It is difficult to resolve urea cycle fluxes without labeling data from metabolites like Gln, which is why the model had to be adjusted to remove urea cycle pathways. Because the central carbon pathways present in the current model account for most carbon flux in prostate metabolism, addition of the urea cycle would likely have minimal impact on current model flux results. For future experiments, increasing the number of biological replicates for each condition would give more accurate mass isotopomer data and may help resolve isotopomer contributions to modeling SSR and allow for the addition of more facets of prostate cancer metabolism.

Chapter 5 : Conclusions and Future Work

5.1 Conclusions

In this work we reviewed the current state of prostate cancer research and introduced the theory behind core metabolic engineering computational and experimental techniques. We then applied these techniques to study the metabolism of prostate cancer cells.

We used prostate cancer cell lines to study how glucose is metabolized under different conditions including androgen sensitive cancer, androgen resistant cancer and androgen sensitive cancer treated with drugs which both promote and inhibit cancer growth. We saw differences in the total enrichment and the mass isotopomer distributions for metabolites under different conditions which gave insight into the activity of metabolic pathways as the disease is treated and progresses.

We also used nonlinear optimization to fit mass isotopomer distributions to isotopic steady state, allowing for steady state metabolic flux analysis. We constructed computational models of central carbon metabolism based on gene annotation information and used the fitted data to run simulations on the models. We found distinct differences in the carbon flux through central pathways across the conditions, which can help focus research and drive development of therapeutic drugs.

5.2 Future work

We hope the introductory chapters of this work will help introduce the fundamentals of metabolic engineering to future laboratory members by providing context, theory and workable examples. It is our aim to also publish the literature review as a resource for information about the history and current state of prostate cancer research.

Future prostate cancer research done with the metabolic engineering toolbox should take these foundational results and use them to either focus in on certain aspects of carbon metabolism in cancer, or expand into different areas of metabolism we have not explored. Central carbon metabolism can be further studied by designing ILEs which characterize certain pathways or repeating ILEs with small adjustments to optimize data acquisition. For example, feeding 1-¹³C glutamine over a longer period of time can determine if TCA metabolites are being replenished via glycolysis or glutaminolysis⁴⁴. Another interesting area of cancer metabolism not studied in this work is nitrogen management. Conducting ILEs using ¹⁵N labeled arginine may give insight into unique ways prostate cancer cells are using nitrogen to help meet energy and biomass requirements. It is possible that combining ¹³C and ¹⁵N labels in the same ILE can give additional flux information, for example resolving urea cycle fluxes which could not be done by feeding U-¹³C glucose.

The extracted lipids from experiments in this work as well as future experiments could be valuable for understanding lipid metabolism. Prior work has shown greater accumulation of lipids in cancer cells⁵¹; ILEs and MFA could be used to

explain this accumulation by identifying flux changes in lipogenesis pathways and their implications in the overall metabolic phenotype. This insight would certainly help the development of more effective treatments.

With respect to the simulations presented in this work, improvements can be made to increase flux accuracy and statistical significance. Using the reported concentrations of unlabeled amino acids in the RPMI medium, input fluxes can be added to account for these additional carbon sources. Once input fluxes are added, multiple simulations should be performed from different starting points in the solution space to ensure convergence on the global minimum SSR. Additional bootstrapping should also be performed to improve confidence intervals on flux values.

Publications

This manuscript is in preparation for publication under the title:

Isotope-Assisted Metabolic Flux Analysis for Prostate Cancer Metabolic Phenotype Characterization.

References

1. Roehrborn, C. G.; Black, L. K., The economic burden of prostate cancer. *BJU Int.* **2011**, *108* (6).
2. Brawley, O. W., Trends in Prostate Cancer in the United States. *J. Natl. Cancer Inst.* **2012**, *2012* (45), 152-156.
3. Kumar, D.; Gupta, A.; Mandhani, A.; Sankhwar, S. N., Metabolomics-derived prostate cancer biomarkers: fact or fiction? *J. Proteome Res.* **2015**, *14* (3), 1455-64.
4. McDunn, J. E.; Li, Z.; Adam, K.-P.; Neri, B. P.; Wolfert, R. L.; Milburn, M. V.; Lotan, Y.; Wheeler, T. M., Metabolomic signatures of aggressive prostate cancer. *Prostate* **2013**, *73* (14), 1547-1560.
5. Damber, J.-E.; Aus, G., Prostate cancer. *Lancet* **2008**, *371* (9625), 1710-1721.
6. Eidelman, E.; Twum-Ampofo, J.; Ansari, J.; Siddiqui, M. M., The Metabolic Phenotype of Prostate Cancer. *Front. Oncol.* **2017**, *7*, 131.
7. Griffin, J., Androgen resistance- the clinical and molecular spectrum. *N. Engl. J. Med* **1992**, *326* (9), 611-618.
8. Sowery, R. D.; So, A. I.; Gleave, M. E., Therapeutic options in advanced prostate cancer: Present and future. *Curr. Urol. Rep.* **2007**, *8* (1), 53-59.
9. Eidelman, E.; Tripathi, H.; Fu, D.-X.; Siddiqui, M. M., Linking cellular metabolism and metabolomics to risk-stratification of prostate cancer clinical aggressiveness and potential therapeutic pathways. *Transl. Androl. Urol.* **2018**.
10. Dakubo, G. D.; Parr, R. L.; Costello, L. C.; Franklin, R. B.; Thayer, R. E., Altered metabolism and mitochondrial genome in prostate cancer. *J. Clin. Pathol.* **2006**, *59* (1), 10-16.
11. Costello, L. C.; Feng, P.; Milon, B.; Tan, M.; Franklin, R. B., Role of zinc in the pathogenesis and treatment of prostate cancer: critical issues to resolve. *Prostate Cancer Prostatic Dis.* **2004**, *7* (2), 111-117.
12. Arnold, R. S.; Sun, C. Q.; Richards, J. C.; Grigoriev, G.; Coleman, I. M.; Nelson, P. S.; Hsieh, C.-L.; Lee, J. K.; Xu, Z.; Rogatko, A.; Osunkoya, A. O.; Zayzafoon, M.; Chung, L.; Petros, J. A., Mitochondrial DNA mutation stimulates prostate cancer growth in bone stromal environment. *Prostate* **2009**, *69* (1), 1-11.
13. Caspi, R.; Foerster, H.; Fulcher, C. A.; Kaipa, P.; Krummenacker, M.; Latendresse, M.; Paley, S.; Rhee, S. Y.; Shearer, A. G.; Tissier, C.; Walk, T. C.; Zhang, P.; Karp, P. D., The MetaCyc Database of metabolic pathways and enzymes and the BioCyc collection of Pathway/Genome Databases. *Nucleic Acids Res.* **2008**, *36* (suppl_1), D623-D631.
14. Kanehisa, M.; Goto, S., KEGG: Kyoto Encyclopedia of Genes and Genomes. *Nucleic Acids Res.* **2000**, *28* (1), 27-30.
15. Zheng, Y.; Sriram, G., Steady-State and Instationary Modeling of Proteinogenic and Free Amino Acid Isotopomers for Flux Quantification. In *Plant Metabolic Flux Analysis: Methods and Protocols*, Dieuaide-Noubhani, M.; Alonso, A. P., Eds. Humana Press: Totowa, NJ, **2014**; pp 155-179.
16. Wiechert, W.; Möllney, M.; Isermann, N.; Wurzel, M.; de Graaf, A. A., Bidirectional reaction steps in metabolic networks: III. Explicit solution and analysis of isotopomer labeling systems. *Biotechnol. Bioeng.* **1999**, *66* (2), 69-85.
17. Sriram, G.; Shanks, J. V., Improvements in metabolic flux analysis using carbon bond labeling experiments: bondomer balancing and Boolean function mapping. *Metab. Eng.* **2004**, *6* (2), 116-132.

18. Antoniewicz, M. R.; Kelleher, J. K.; Stephanopoulos, G., Elementary metabolite units (EMU): A novel framework for modeling isotopic distributions. *Metab. Eng.* **2007**, *9* (1), 68-86.
19. Sriram, G. Flux analysis in central carbon metabolism in plants : ¹³C NMR experiments and analysis. **2004**.
20. Press, W. H.; Teukolsky, S. A.; Vetterling, W. T.; Flannery, B. P., *Numerical recipes 3rd edition: The art of scientific computing*. Cambridge university press: **2007**.
21. Emwas, A. H., The strengths and weaknesses of NMR spectroscopy and mass spectrometry with particular focus on metabolomics research. *Methods Mol. Biol.* **2015**, *1277*, 161-93.
22. Tolstikov, V. V.; Fiehn, O.; Tanaka, N., Application of Liquid Chromatography-Mass Spectrometry Analysis in Metabolomics. In *Metabolomics: Methods and Protocols*, Weckwerth, W., Ed. Humana Press: Totowa, NJ, **2007**; pp 141-155.
23. Fernandez, C. A.; Des Rosiers, C.; Previs, S. F.; David, F.; Brunengraber, H., Correction of ¹³C mass isotopomer distributions for natural stable isotope abundance. *J. Mass Spectrom.* **1996**, *31* (3), 255-62.
24. Millard, P.; Letisse, F.; Sokol, S.; Portais, J.-C., IsoCor: correcting MS data in isotope labeling experiments. *Bioinformatics* **2012**, *28* (9), 1294-1296.
25. Midani, F. S.; Wynn, M. L.; Schnell, S., The importance of accurately correcting for the natural abundance of stable isotopes. *Anal. Biochem.* **2017**, *520*, 27-43.
26. Denmeade, S. R.; Isaacs, J. T., A History of Prostate Cancer Treatment. *Nat. Rev. Cancer* **2002**, *2* (5), 389-396.
27. Trock, B. J., Application of Metabolomics to Prostate Cancer. *Urol. Oncol.* **2011**, *29* (5), 572-581.
28. Sreekumar, A.; Poisson, L. M.; Rajendiran, T. M.; Khan, A. P.; Cao, Q.; Yu, J.; Laxman, B.; Mehra, R.; Lonigro, R. J.; Li, Y.; Nyati, M. K.; Ahsan, A.; Kalyana-Sundaram, S.; Han, B.; Cao, X.; Byun, J.; Omenn, G. S.; Ghosh, D.; Pennathur, S.; Alexander, D. C.; Berger, A.; Shuster, J. R.; Wei, J. T.; Varambally, S.; Beecher, C.; Chinnaiyan, A. M., Metabolomic Profiles Delineate Potential Role for Sarcosine in Prostate Cancer Progression. *Nature* **2009**, *457* (7231), 910-914.
29. Jentzmik, F.; Stephan, C.; Miller, K.; Schrader, M.; Erbersdobler, A.; Kristiansen, G.; Lein, M.; Jung, K., Sarcosine in Urine after Digital Rectal Examination Fails as a Marker in Prostate Cancer Detection and Identification of Aggressive Tumours. *Eur. Urol.* **2010**, *58* (1), 12-18.
30. Tessem, M.-B.; Swanson, M. G.; Keshari, K. R.; Albers, M. J.; Joun, D.; Tabatabai, Z. L.; Simko, J. P.; Shinohara, K.; Nelson, S. J.; Vigneron, D. B.; Gribbestad, I. S.; Kurhanewicz, J., Evaluation of Lactate and Alanine as Metabolic Biomarkers of Prostate Cancer Using (1)H HR-MAS Spectroscopy of Biopsy Tissues. *Magn. Reson. Med.* **2008**, *60* (3), 510-516.
31. van Asten, J. J. A.; Cuijpers, V.; Hulsbergen-van de Kaa, C.; Soede-Huijbregts, C.; Witjes, J. A.; Verhofstad, A.; Heerschap, A., High resolution magic angle spinning NMR spectroscopy for metabolic assessment of cancer presence and Gleason score in human prostate needle biopsies. *Magn. Reson. Med.* **2008**, *21* (6), 435-442.
32. Thysell, E.; Surowiec, I.; Hörnberg, E.; Crnalic, S.; Widmark, A.; Johansson, A. I.; Stattin, P.; Bergh, A.; Moritz, T.; Antti, H.; Wikström, P., Metabolomic Characterization of Human Prostate Cancer Bone Metastases Reveals Increased Levels of Cholesterol. *PLOS One* **2010**, *5* (12), e14175.
33. Thomas, T.; Thomas, T. J., Polyamine metabolism and cancer. *J. Cell. Mol. Med.* **2003**, *7* (2), 113-26.

34. Meller, S.; Meyer, H.-A.; Bethan, B.; Dietrich, D.; Maldonado, S. G.; Lein, M.; Montani, M.; Reszka, R.; Schatz, P.; Peter, E.; Stephan, C.; Jung, K.; Kamlage, B.; Kristiansen, G., Integration of tissue metabolomics, transcriptomics and immunohistochemistry reveals ERG- and gleason score-specific metabolomic alterations in prostate cancer. *Oncotarget* **2016**, *7* (2), 1421-1438.
35. Ellis, J. K.; Athersuch, T. J.; Thomas, L. D. K.; Teichert, F.; Pérez-Trujillo, M.; Svendsen, C.; Spurgeon, D. J.; Singh, R.; Järup, L.; Bundy, J. G.; Keun, H. C., Metabolic profiling detects early effects of environmental and lifestyle exposure to cadmium in a human population. *BMC Med.* **2012**, *10* (1), 61.
36. Johnson, C. H.; Ivanisevic, J.; Siuzdak, G., Metabolomics: beyond biomarkers and towards mechanisms. *Nat. Rev. Mol. Cell Biol.* **2016**, *17* (7), 451-459.
37. Johnson, C. H.; Dejea, C. M.; Edler, D.; Hoang, L. T.; Santidrian, A. F.; Felding, B. H.; Cho, K.; Wick, E. C.; Hechenbleikner, E. M.; Uritboonthai, W.; Goetz, L.; Casero, R. A.; Pardoll, D. M.; White, J. R.; Patti, G. J.; Sears, C. L.; Siuzdak, G., Metabolism links bacterial biofilms and colon carcinogenesis. *Cell Metab.* **2015**, *21* (6), 891-897.
38. Dejea, C. M.; Wick, E. C.; Hechenbleikner, E. M.; White, J. R.; Mark Welch, J. L.; Rossetti, B. J.; Peterson, S. N.; Snesrud, E. C.; Borisy, G. G.; Lazarev, M.; Stein, E.; Vadivelu, J.; Roslani, A. C.; Malik, A. A.; Wanyiri, J. W.; Goh, K. L.; Thevambiga, I.; Fu, K.; Wan, F.; Llosa, N.; Housseau, F.; Romans, K.; Wu, X.; McAllister, F. M.; Wu, S.; Vogelstein, B.; Kinzler, K. W.; Pardoll, D. M.; Sears, C. L., Microbiota organization is a distinct feature of proximal colorectal cancers. *Proc. Natl. Acad. Sci. U.S.A.* **2014**, *111* (51), 18321-18326.
39. Cai, T.; Tessarolo, F.; Caola, I.; Piccoli, F.; Nollo, G.; Caciagli, P.; Mazzoli, S.; Palmieri, A.; Verze, P.; Malossini, G.; Mirone, V.; Bjerklund Johansen, T. E., Prostate calcifications: A case series supporting the microbial biofilm theory. *Investig. Clin. Urol.* **2018**, *59* (3), 187-193.
40. Alimirah, F.; Chen, J.; Basrawala, Z.; Xin, H.; Choubey, D., DU-145 and PC-3 human prostate cancer cell lines express androgen receptor: Implications for the androgen receptor functions and regulation. *FEBS Lett.* **2006**, *580* (9), 2294-2300.
41. Everley, P. A.; Bakalarski, C. E.; Elias, J. E.; Waghorne, C. G.; Beausoleil, S. A.; Gerber, S. A.; Faherty, B. K.; Zetter, B. R.; Gygi, S. P., Enhanced Analysis of Metastatic Prostate Cancer Using Stable Isotopes and High Mass Accuracy Instrumentation. *J. Proteome Res.* **2006**, *5* (5), 1224-1231.
42. Wright, J. L.; Stanford, J. L., Metformin use and prostate cancer in Caucasian men: results from a population-based case-control study. *Cancer Causes Control* **2009**, *20* (9), 1617-1622.
43. Fendt, S. M.; Bell, E. L.; Keibler, M. A.; Davidson, S. M.; Wirth, G. J.; Fiske, B.; Mayers, J. R.; Schwab, M.; Bellinger, G.; Csibi, A.; Patnaik, A.; Blouin, M. J.; Cantley, L. C.; Guarente, L.; Blenis, J.; Pollak, M. N.; Olumi, A. F.; Vander Heiden, M. G.; Stephanopoulos, G., Metformin decreases glucose oxidation and increases the dependency of prostate cancer cells on reductive glutamine metabolism. *Cancer Res.* **2013**, *73* (14), 4429-38.
44. Metallo, C. M.; Gameiro, P. A.; Bell, E. L.; Mattaini, K. R.; Yang, J.; Hiller, K.; Jewell, C. M.; Johnson, Z. R.; Irvine, D. J.; Guarente, L.; Kelleher, J. K.; Vander Heiden, M. G.; Iliopoulos, O.; Stephanopoulos, G., Reductive glutamine metabolism by IDH1 mediates lipogenesis under hypoxia. *Nature* **2011**.
45. Hevia, D.; Gonzalez-Menendez, P.; Fernandez-Fernandez, M.; Cueto, S.; Rodriguez-Gonzalez, P.; Garcia-Alonso, J. I.; Mayo, J. C.; Sainz, R. M., Melatonin Decreases Glucose Metabolism in Prostate Cancer Cells: A (13)C Stable Isotope-Resolved Metabolomic Study. *Int. J. Mol. Sci.* **2017**, *18* (8), 1620.

46. Brindle, K. M.; Bohndiek, S. E.; Gallagher, F. A.; Kettunen, M. I., Tumor imaging using hyperpolarized ¹³C magnetic resonance spectroscopy. *Magn. Reson. Med.* **2011**, *66* (2), 505-519.
47. Nelson, S. J.; Kurhanewicz, J.; Vigneron, D. B.; Larson, P. E. Z.; Harzstark, A. L.; Ferrone, M.; van Criekinge, M.; Chang, J. W.; Bok, R.; Park, I.; Reed, G.; Carvajal, L.; Small, E. J.; Munster, P.; Weinberg, V. K.; Ardenkjaer-Larsen, J. H.; Chen, A. P.; Hurd, R. E.; Odegardstuen, L.-I.; Robb, F. J.; Tropp, J.; Murray, J. A., Metabolic Imaging of Patients with Prostate Cancer Using Hyperpolarized [1-(¹³C)]Pyruvate. *Sci. Transl. Med.* **2013**, *5* (198), 198ra108-198ra108.
48. van Winden, W.; Schipper, D.; Verheijen, P.; Heijnen, J., Innovations in generation and analysis of 2D [(¹³C),(¹H)] COSY NMR spectra for metabolic flux analysis purposes. *Metab. Eng.* **2001**, *3* (4), 322-43.
49. Riganti, C.; Gazzano, E.; Polimeni, M.; Aldieri, E.; Ghigo, D., The pentose phosphate pathway: An antioxidant defense and a crossroad in tumor cell fate. *Free Radic. Biol. Med.* **2012**, *53* (3), 421-436.
50. Mukherji, D.; Pezaro, C. J.; De-Bono, J. S., MDV3100 for the treatment of prostate cancer. *Expert Opin. Investig. Drugs* **2012**, *21* (2), 227-233.
51. Wu, X.; Daniels, G.; Lee, P.; Monaco, M. E., Lipid metabolism in prostate cancer. *Am. J. Clin. Exp. Urol.* **2014**, *2* (2), 111-120.